Characterization of Soft Polymers and Gels using the Pressure-Bulge Technique

Thesis by

Winston Paul Jackson

In Partial Fulfillment of the Requirements

for the Degree of

Doctor of Philosophy

California Institute of Technology

Pasadena, California

2008

(Defended May 27, 2008)

Acknowledgments

I would first like to acknowledge my family, for without them I would not have gotten the opportunity to write this document or receive this degree. To my mom, my sister, and my brother: your love and support have been overwhelming, and for it, I humbly thank you. I love you each of you. Secondly, I would like to dedicate my thesis to four very important women that have passed away since I moved to California to begin this process. They are Rosie Jackson, Bertha Williams, Celia B. Hart, and Johnnie M. Watts. My only regret is that you all could not be here for this moment for each of you know that you played no small role in this accomplishment. I hope I made you proud.

I would next like to acknowledge my advisor, Prof. G. Ravichandran, for allowing me an opportunity to work in his lab. Thank you for your patience and understanding. I would also like to thank the members of my thesis committee, Profs. Daraio, Bhattacharya, and Knauss for making this moment possible. Lastly, I would like to thank all of the members in the Ravichandran lab that have preceded me in departure and those that still remain once I leave. It has truly been a pleasure working with you.

Jen and Christian: I must sincerely thank the two of you, for without your friendship, getting through Caltech would have been a definite impossibility. I enjoyed working and learning with you, and I hope to continue to do that for many years to come.

Don: Thanks for all of the late nights and the listening ear. You are truly one of the best friends anyone could ask for.

Stacey: I will miss you and our talks. You are a brilliant scientist and the hardest working person that I have ever met. I hope to continue our convos in the future.

Linda: You are awesome...the best. I will miss you and Aiden, so don't forget about me when

I'm gone!

Luz: You have been a great friend. I hope we can continue our long talks when I leave Caltech.

I would also like to say that it has been a pleasure meeting and getting to know the following people: Chris K., Mike M., Chris and Sarah A., Daniel C., Ivan M., and Lydia T. I wish you all the best in your endeavors.

I would like to acknowledge the Minority Student Education office and the Student Affairs staff for helping to make this process just a little easier.

Lastly, I want to thank my friends for always being there for me, and while you are last on this list, you are definately first in my heart. To Terrence, Arthur, Merlin, Honey, Jennifer C., Tenky, Raven, Mekeeda, and Anthony: thanks for always standing by me. I love each of you.

In loving memory of my father, Bobby Gene Jackson.

Abstract

A method to characterize the bulk hydrated properties of soft polymers and hydrogels, whose moduli are in the low MPa regime, using the pressure-bulge technique is presented. The pressure-bulge technique has been used extensively in the characterization of thin films, particularly for the case of metals. The extension of the plane-strain and circular bulge techniques to determine the Young's modulus and Poisson's ratio of bulk latex and silicone rubber sheets are shown here, in addition to the viscoelastic behavior of 5% agarose gel in the time domain using relaxation tests.

The membranes are clamped between two stainless steel plates that are connected to a liquid pressure chamber. A syringe connected to a linear actuator causes changes in the pressure and displacement, and a pressure sensor and confocal displacement sensor are used to monitor these changes in real time. The theory presented converts the measured pressure and displacement data into stress and stretch data, using a geometrically nonlinear analysis, and the elastic/viscoelastic properties are then determined from this data.

The results from the bulge tests are compared with data from uniaxial tension tests on hydrated specimens, and the data comparison with respect to each of the materials tested show good agreement between the two measurements. These results show promise regarding the use of pressure-displacement techniques to characterize other soft material systems, including biological polymers and tissues, as well as cell-to-matrix and cell-to-cell interactions under varying mechanical loading conditions of cell substrates.

Contents

List of Figures

List of Tables

Chapter 1

Introduction

1.1 Motivation

Over the past several years, research in the field of cell biology has tended to become more quantitative, and as a result the field of biomechanics has gained prominence in the mechanics community [35, 42]. Early work in the field of cell mechanics has convincingly shown that the extracellular mechanical environment plays a significant role in cellular processes, thereby creating a need to understand the various implications of these phenomena [35, 42]. However, as research in cell and tissue mechanics expands, so does the need to develop experimental techniques that are both consistent with characterization methods already existing in mechanics, but which also promote biocompatibility and accurately mimic *in vivo* mechanical and biochemical conditions [14, 15, 28]. The marriage of these two requirements has offered a difficult challenge for researchers drawing from expertise in both biology and mechanics. Even so, there have been many techniques developed in an attempt to bridge this divide. These techniques include the response of adherent cells to fluid shear stress; the deformation of single cells using micropipette aspiration, optical and magnetic tweezers, and atomic force microscopy; embedded particle tracking for measurement of cell migration; and lastly, cell-substrate (extra-cellular matrix) deformation techniques [35]. The latter provides the motivation for this work.

Cell-substrate deformation techniques are usually classified based upon how the load or deformation is applied. In this sense, two types of methodologies popular today. The first involve substrates

that are deformed only in-plane by applying uniaxial or biaxial tension [20, 39]. The second kind subjects clamped or bonded substrates to transverse loading over some geometry and have been referred to as inflation tests [14, 28]. By definition, these latter test methods do not provide a uniaxial stress state, but for circular and square geometries an equi-biaxial stress state exists in the membranes. Both experimental configurations have experienced limitations in fully achieving their intended purposes. For the former, these include the inability to measure both displacement (strain) and force (stress) simultaneously while maintaining a biocompatible environment in which cells can grow and live, as well as, the inability to accurately mimic *in vivo* loading conditions for relevant tissue and cell types. However, due to the lack of out-of-plane motions of the specimens, this technique promotes *in situ* cell imaging. In the case of the inflation tests, they are inherently easier in providing a biocompatible environment and can accurately mimic *in vivo* loading conditions (particularly for arterial cells and tissues subject to transverse pressure loading), but have not been able to fully develop as a mechanics test because of limitations in measuring displacement and developing stress and strain relations from the measured parameters. Also, as expected, *in situ* cell imaging for this technique is more difficult because of out-of-plane motions which constantly change the focusing length of any imaging technique.

Another commonly used test, called the pressure-bulge technique, has been shown to be successful for the mechanical characterization of thin-films made of metal, ceramics, or stiff polymers in the elastic, viscoelastic, and/or plastic regimes [19, 32]. The thin-films usually studied using this technique have thicknesses less than 10 μm, which causes their in-plane properties to deviate significantly from those of the bulk material due to microstructural effects [19]. The basis of the procedure requires applying a known transverse pressure to a clamped specimen and simultaneously measuring the deflection in a manner similar to the inflation tests mentioned above. Using a geometric theory based on the membrane approximation and Kirchhoff's plate theory, several researchers have proposed analytical models for this type of setup. These models have been used extensively to determine residual film stress, Young's modulus, and Poisson's ratio of thin-film materials.

The overall goal of this project is to develop a theory and method consistent with the traditional

bulge test technique that can be used as a cell-substrate deformation testing apparatus. In this way, we seek to combine the methodology used in inflation tests for biological applications with the theory from the bulge test in an effort to more rigorously characterize the mechanical behavior of cell-matrix systems using mechanics parameters. In the following section, an overview of the literature is presented, which gives a chronological review of the evolution of both the bulge and inflation tests.

1.2 Literature Review

1.2.1 Pressure-Bulge Technique for Thin-Film Characterization

The pressure-bulge test was one of the earliest techniques used to characterize the behavior of small structures, and in 1959, J.W. Beams published a book on the mechanical properties of thin films of gold and silver [2]. In his work, Beams used a circular orifice with a transverse punch to apply pressure across a membrane [2]. Due to the lack of advanced micromachining technology, many problems existed for the pioneering experimental setup reported by Beams, including but not limited to accurate control of specimen geometry and debonding or slipping at the boundaries. However, advances in micromachining technology and imaging capabilities over the past four decades have reduced many of these early challenges. In the years to follow, many researchers successfully utilized the circular bulge configuration to characterize thin metal films [1, 33, 34]. In 1987, Allen et al. [1] characterized polyimide films on silicon dioxide substrates using the pressure-bulge technique with a square orifice, and shortly thereafter, Tabata et al. [33] characterized silicon nitride using a rectangular membrane with a multilayer assembly. For the latter, an elastic solution that provided the pressure as a function of the center-point displacement was proposed using energy minimization. The general form of the pressure displacement relation used to interpret the bulge test results is

$$P = \frac{C_1 \sigma_0 t}{a^2} h + \frac{C_2 E t}{a^4} h^3, \tag{1.1}$$

where σ_0 is the residual tensile film stress, t is the film thickness, h is the center-point deflection, a is the membrane half-length (for rectangular samples it is the half-length of the shorter dimension and for circular samples it is the radius), E is the Young's modulus of the material, and C_1 and C_2 are constants that have been determined using finite element analysis or energy minimization for different geometric configurations. It should be noted that C_2 also depends on the material's Poisson's ratio and (1.1) is only valid for linearly elasticity.

The work conducted by W.D. Nix and his students in 1992 [31, 30, 37] has contributed to the widespread use of the bulge test to characterize thin films accurately. Small and Nix [31] provided more in-depth analysis regarding many of the issues that arise with the bulge technique, including film buckling and non-flat initial conditions. Vlassak and Nix [37] also showed for the first time that two bulge configurations could be used in tandem to determine Young's modulus and Poisson's ratio uniquely, and that a plane-strain analytical solution results for high in-plane aspect ratios. In 1995, Breton and Knauss analyzed the error limitations associated with the determination of Young's modulus and Poisson's ratio for rectangular membranes using a solution obtained by energy minimization [3, 4]. That same year, D. Maier-Schneider et al. [22] provided new values for the parameters C_1 and C_2 found in (1.1) by using a new minimization technique that included more terms in the displacement functions used by Tabata, and thereby claimed better accuracy than the values provided by Tabata, Nix, and others. In 1998, Ziebart et al. [43] expanded the study of the plane-strain bulge test configuration and provided a model that allowed for researchers to study films that had compressive residual stresses without having to include them in a multilayer arrangement. This work also provided a model that included flexural rigidity in which case the membrane assumption no longer holds. Figure 1.1 shows a picture of the deformed plane-strain 3-dimensional profile taken from their work.

Most bulge test configurations use interferometry as a standard full-field displacement measuring technique. Interferometric images taken from Walmsley et al. [38] are shown in Figures 1.2 (a) and (b) for the square and rectangular bulge configurations, respectively. Figure 1.2 (c) shows a plot of the out-of-plane displacement along the membrane center-lines for both configurations. Because

white and dark fringes represent the constructive and destructive interference of reflected light from the sample, each fringe is related to half the wavelength of the laser light used. This allows researchers to relate the fringe count for images acquired during deformation to the out-of-plane displacement. Some researchers, however, began to move away from the common use of interferometric imaging techniques in the late 1990s for other displacement measuring techniques such as laser scanning and single-point methods [17, 18, 24, 23]. Laser scanning reflection allows for a film curvature measurement, as opposed to film displacement, which can help with decreasing errors due to initial film heights [18]. It is noted extensively in the literature that the initial state of the membrane is crucial in obtaining accurate results using any pressure-deflection technique [31]. Figure 1.3 is taken from Small and Nix [31] and schematically demonstrates the cases where membranes can either wrinkle in their undeformed state or have an initial height prior to loading, conditions whereby the flatness requirement for use of (1.1) is violated.

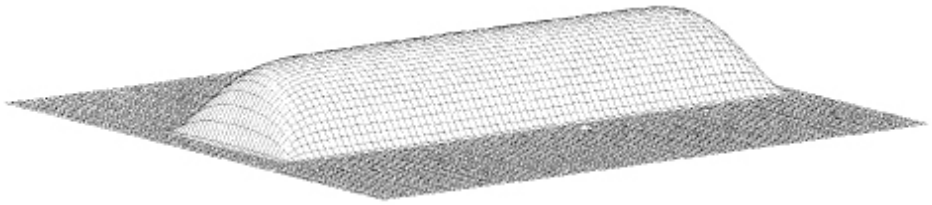

Figure 1.1: Deformed 3-dimensional profile of the plane-strain bulge configuration (from Ziebart et al. [43])

Much of the work subsequent to 1998, sought to use the bulge test to characterize more novel materials, such as shape memory alloys and other temperature sensitive metals, under dynamic conditions [13, 16, 24, 23]. In 2002 Kalkman et al. [17] extended the bulge test to the study of thin-film plasticity in polycrystalline aluminum by looking at the transient creep behavior of films under constant stress. Up until this point, most bulge tests were used to monotonically load and unload specimens, but time- and frequency-dependent tests had become more commonplace. By this point in time, the bulge test had been used to characterize many standard MEMS materials, most commonly silicon-nitride, and the versatility of the technique had been highlighted throughout the literature.

In 2003, Mitchell et al. [25] reviewed much of the previous work conducted using the bulge test and found several discrepancies among the models and experimental techniques. They observed that the values C_1 and C_2 from (1.1) were given differently by several researchers, as shown in Table 1.2.1, highlighting the disadvantage in using the elastic models determined from finite element and energy minimization techniques over analytical formulations. Additionally, they pointed out a deviation between modulus and residual stress values that were determined from film bulging into the orifice and film bulging away from the orifice. These two loading configurations are shown schematically in Figure 1.4. They concluded that the experiments fit better with the analytical solutions for film bulging into the orifice, and that film bulging away from the orifice loses accuracy as the displacement increases. This discrepancy is believed to be due to different boundary conditions for the two cases, in which the latter exhibits limitations in maintaining a clamped boundary under large pressures. Conversely, in 2004, Edwards et al. [10] provided some of the first work that successfully compared the accuracy of the bulge test with a uniaxial tension test for thin-films. They were able to show a very good correlation between the bulge test and tension results, obtaining modulus values for silicon nitride of 258±1 GPa and 257±5 GPa, respectively, from the two apparatuses. It is not clear, however, whether during their bulge test experiments they bulged away from or toward the orifice.

Bulge Geometry	*Authors*	C_1	$C_2(1-\nu)$
Circular	Beams (1959)	4.0	2.67
	Pan et al. (1990)	4.0	$2.67(1.026+0.233\nu)^{-1}$
	Small and Nix (1992)	4.0	(7-ν)/3
Square	Allen et al. (1987)	3.04	1.473(1-0.272ν)
	Tabata et al. (1989)	3.04	1.473(1-0.272ν)
	Pan et al. (1990)	3.41	1.37(1.075-0.292ν)
	Vlassak and Nix (1992)	3.393	$(0.8+0.062\nu)^3$
	Maier-Schneider et al. (1995)	3.45	1.994(1-0.271ν)
Rectangular	Tabata et al. (1989)	1.552	[30/(1+ν)][0.035-(16/(800-89ν))]
	Vlassak and Nix (1992)	2	8/[6(1+ν)]

Table 1.1: Constants C_1 and C_2 in the pressure-displacement relation Eq. (1.1) for various bulge geometries (from Mitchell et al. [25])

The evolution of the bulge test as a characterization tool was brought to an apex by the work presented by Xiang et al. [41] in 2005. In this publication, a geometric theory was presented that allowed for the derivation of an analytical solution for stress and strain in a high aspect ratio

rectangular membrane in which one in-plane dimension is at least four times the length of the other. As a result, the authors were able use these relations to characterize thin-films outside the regime of linear elasticity, since the derivations were independent of the material constitutive behavior.

The aforementioned work led to the more recent publication in 2007 by Larson et al. [21] in which bulk polyethylene and polypropylene membranes were characterized using circular and square bulge test configurations. This was the only publication over the past several years in which researchers utilized the equations of the bulge test to characterize membranes that were not in the thin-film regime. Additionally, this work used an LVDT (linear variable displacement transducer) to measure the center-point film displacement, which is a contact measuring technique. Other researchers use optical techniques that usually require a great deal of sample reflectivity to measure the displacement in real-time, and polymers (unlike metals) usually lack this optical characteristic. While contact measurements for this type of test can induce significant error for low-pressure measurements of soft films, the authors do not report any inaccuracies incurred by using an LVDT. While much of the utility of the bulge test has found its way into thin-film mechanics for MEMS applications, this latest work highlights the potential of the method to extend beyond the class of thin-film materials, which speaks directly to the motivation and relevance of the work presented here.

1.2.2 Inflation Test for Large Deformation of Soft Materials

The concept of membrane inflation for large deformation analysis of elastomers has been around since 1944, however the idea of using the test in the characterization of soft tissues was first proposed in 1979 by Wineman et al [40]. Though no actual experiments were conducted, this work proposed using a strain energy function in conjunction with a kinematic description of axisymmetric membrane inflation to develop a model for large deformations of biological membranes. After this, there appear to be relatively few publications with regard to the membrane inflation test until 1992 when W. Feng published on the viscoelastic behavior of elastomers using results from an inflation test [11].

In 1994 Hsu et al. [15] revisited the membrane inflation test by considering the relations of finite elasticity under the loading configuration given by an axisymmetric transverse pressure. Unlike much

of the previous work, this work presented experimental data that validated their large deformation model. The authors noted the importance and relevance of an inflation test for the characterization of natural tissues and other biological materials whose specimen geometries cannot be manipulated for use in other tests like uniaxial tension and compression or torsion. In the following year, Hsu et al. [14] adopted a triplane camera system to track markers placed on a membrane in an effort to accurately determine the stretches in the meridional and circumferential directions during membrane inflation. These experiments were conducted on thin sheets of polyisoprene, as well as on a sample of healthy contra-lateral carotid artery and a fusiform aneurysm. This work provided the first successful use of the membrane inflation test in determining stress and strain data for biological membranes.

In 2004, Shukla et al. [29] used a setup similar to an inflation test, though they did not refer to it as such, to look at the behavior of cultured endothelial cells under cyclic substrate deflection. In this study, the authors were specifically concerned with enzymatic activity and network formulation of the cell culture and were not interested in determining any constitutive behavior of this biological system. Similarly, more recent work published in 2007 by Selby and Shannon [28] also looked at cell behavior under cyclic substrate deflection. However, this work was more concerned with quantifying the cell-to-cell behavior of a layer of epithelial cells under finite cyclic deformations. Again, this work did not provide much insight into the constitutive behavior of this system, but the authors did conduct six-cycle inflation experiments to observe a decreasing inter-cycle hysteretic effect in the load-deformation curve, inferring some type of rheological behavior of the system due to cell contact at the cell-to-cell junctions. Figures 1.5 and 1.6 are extracted from Selby's and Shannon's 2007 publication, and the former shows schematically the experimental procedure used in their study while the latter shows the cyclic hysteresis curves for the membrane alone (Figure 1.6(a)) and the membrane with a layer of cultured cells (Figure 1.6(b)).

1.3 Approach and Objectives

The membrane inflation and pressure-bulge techniques both operate using the same principle, however, there are differences between the materials traditionally characterized using each test. The membrane inflation test has been primarily used on bulk specimens of elastomers and other soft materials, whereas the pressure-bulge technique has been applied to thin-films made of metals, ceramics, and stiff polymers. As a result, most membrane inflation models for soft materials have been formulated for highly nonlinear geometric behavior. However, the models developed to characterize thin films are usually geometrically constrained in terms of the out-of-plane displacement. In any case, these differences are artificial, and for the majority of this study, geometric models based on kinematic assumptions and force equilibrium will be used. This allows stress and strain to be derived without regard to the constitutive behavior of the material.

The membrane inflation test has shown much promise in the evaluation of the large deformation behavior of elastomers, tissues, and biological systems. However, the major limitation in the technique thus far is the inability to quantify results with parameters commonly used in mechanics, such as elastic and time-dependent moduli. This, however, has been one of the great strengths of the pressure-bulge technique for thin-film characterization. If mechanical properties are extracted in conjunction with observed biological changes under dynamic mechanical conditions, then the marriage of mechanics and biology could profit greatly. The present work is intended to make progress in this direction.

The previous sections have provided an overview of the project motivation and relevant literature. In the following chapters, the development of a pressure-bulge technique with the goal of conducting experiments on soft polymers, including biologically relevant hydrogels, is described. In Chapter 2, the relevant theory for the plane-strain and circular bulge techniques is described under several conditions, including for initially non-flat specimens and viscoelastic behavior. Next, Chapter 3 describes the experimental setup used in the present study in detail. In Chapter 4 results from the characterization of latex and silicone rubber sheets are presented in an effort to validate the theory and determine the accuracy of the experimental facility with comparisons to tension tests. This is

followed by Chapter 5 in which the pressure-bulge technique is used to elucidate the viscoelastic behavior of agarose gels. Lastly, Chapter **??** provides a summary of the work presented in the previous chapters, and concludes with a discussion regarding future work in this area.

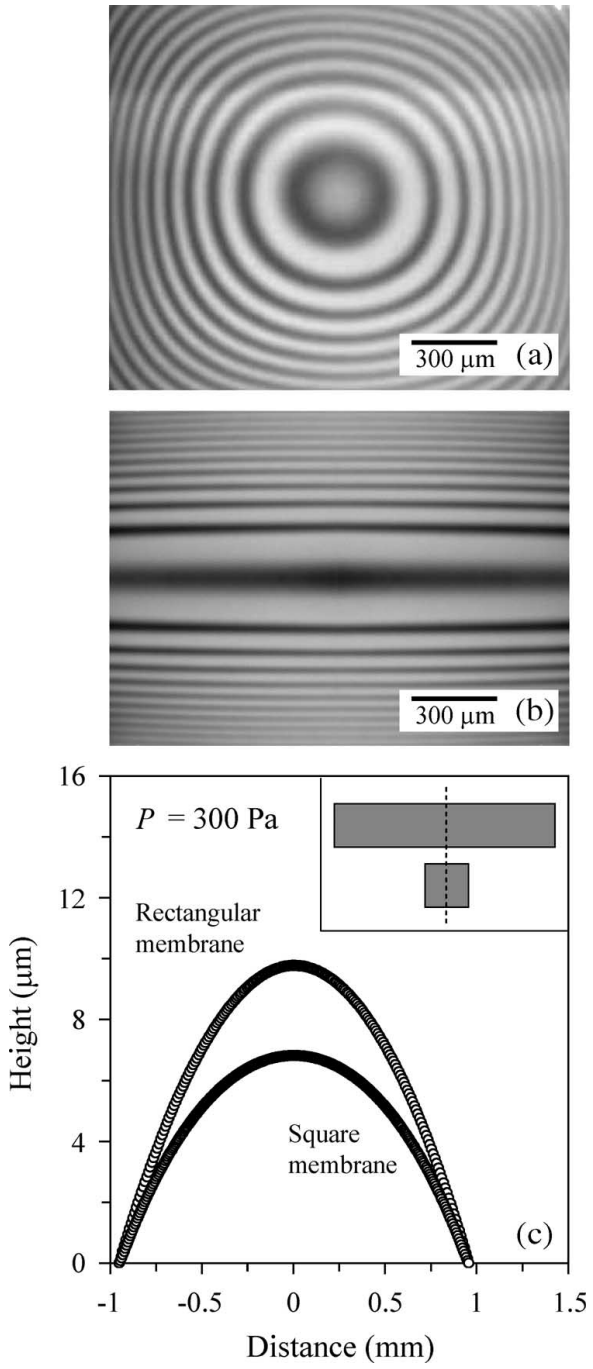

Figure 1.2: (a) and (b) Interferometric fringes for square and rectangular bulge configurations, resp., (c) and displacement profiles along the membrane center-lines for each case (from Walmsley et al. [38])

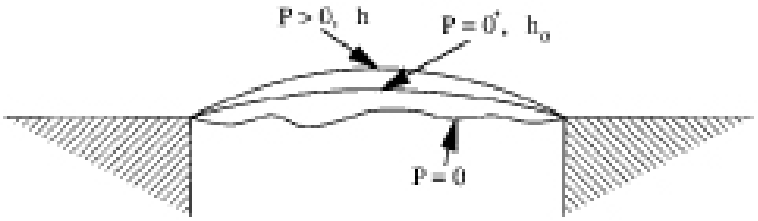

Figure 1.3: Schematic of a membrane in three different kinematic states: a wrinkled state for zero pressure, an initial height for pressures slightly greater than zero, and a deformed height for monotonically increasing pressures (from Small and Nix [31])

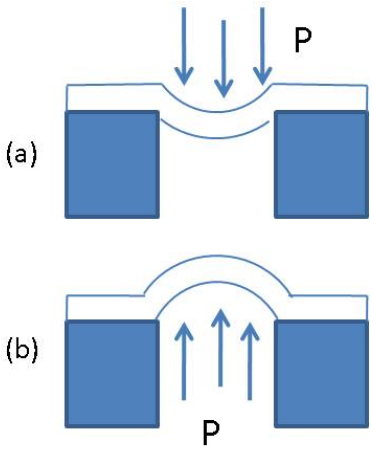

Figure 1.4: Schematic of two different loading configurations used in the pressure-bulge technique (a) deflection of the membrane into the orifice and (b) deflection of the membrane away from the orifice

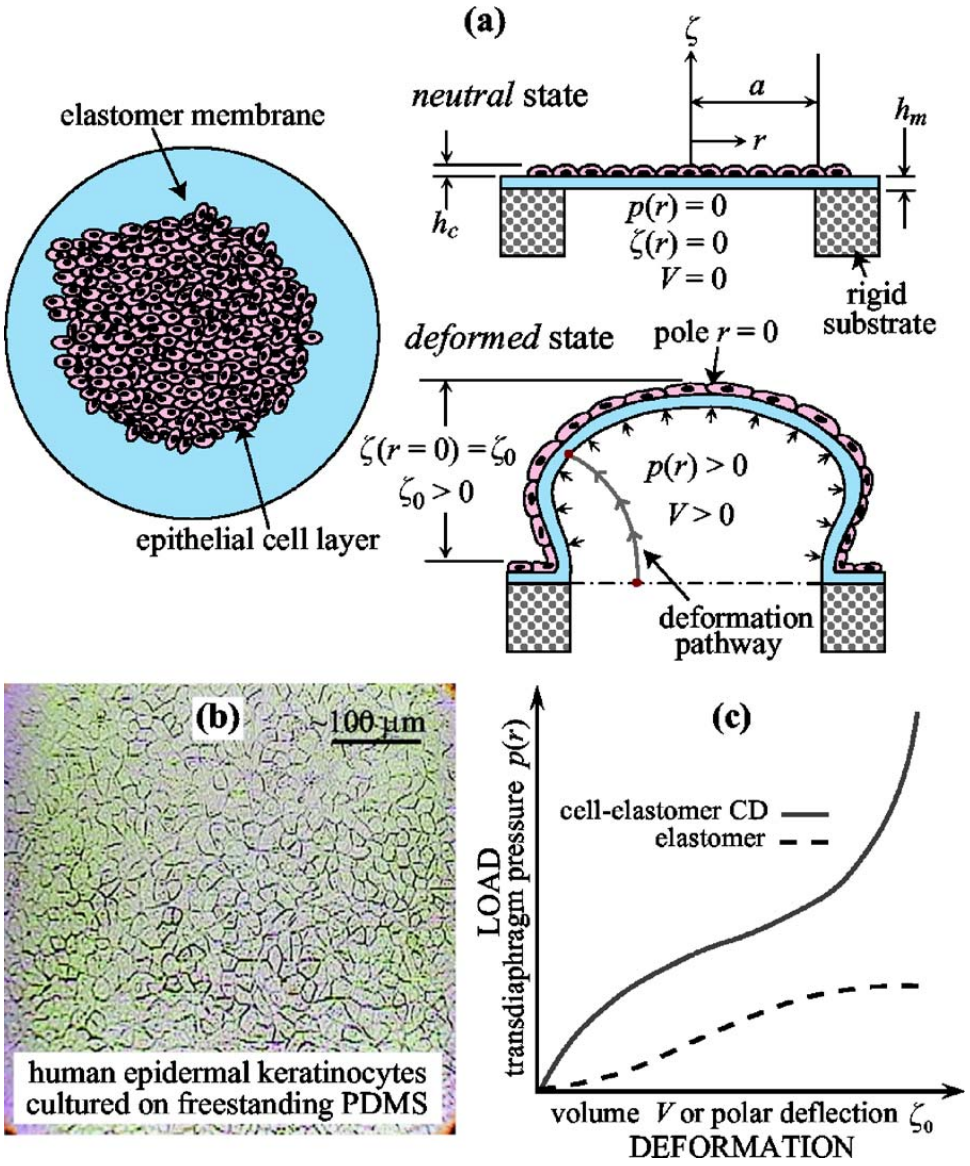

Figure 1.5: Illustrative overview of the membrane inflation test for cell-substrate studies (from Selby and Shannon [28])

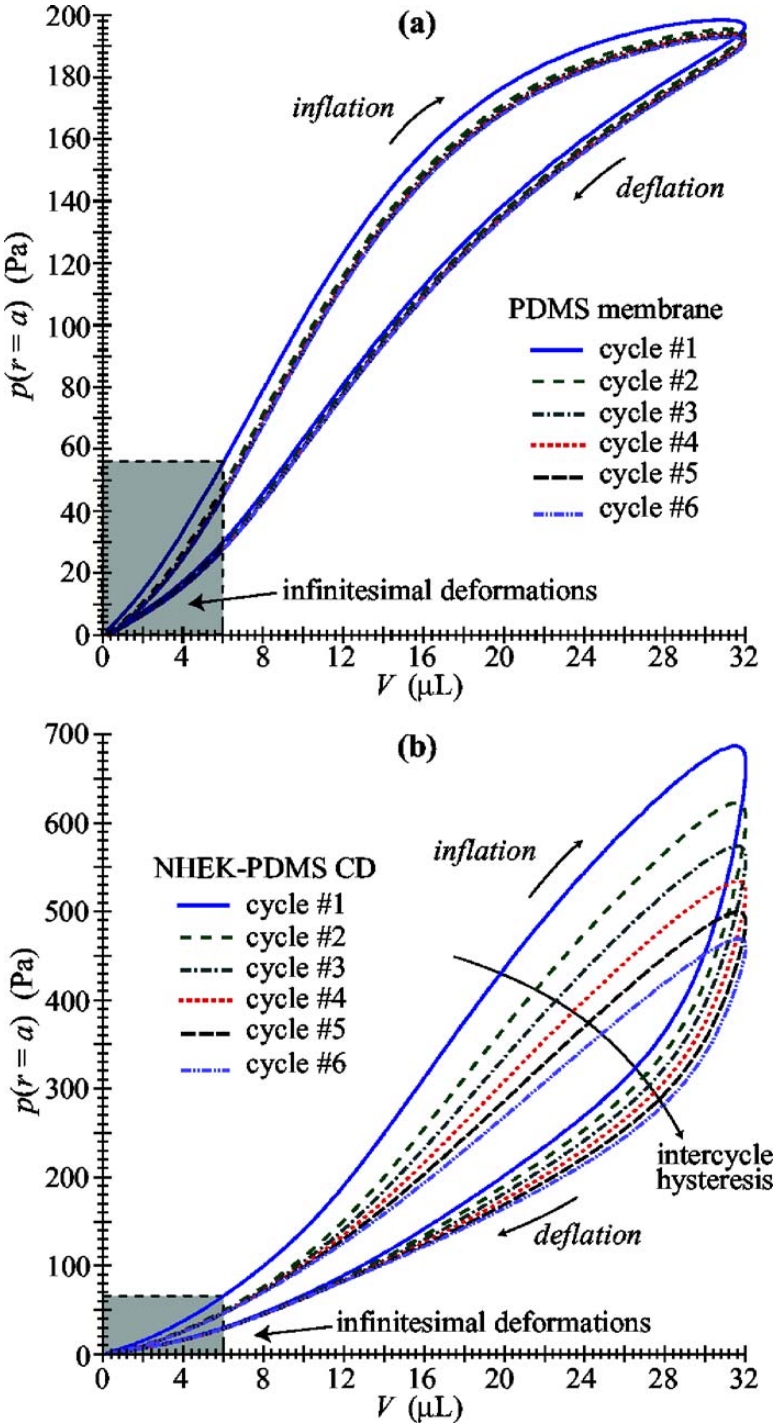

Figure 1.6: (a) Cyclic hysteresis curves for a single PDMS membrane and (b) cyclic hysteresis curves for a PDMS membrane with a layer of cultured cells using the membrane inflation test(from Selby and Shannon [28])

Chapter 2

Membrane Theory

In this chapter the theory of a clamped membrane under transverse pressure will be developed for both the plane-strain and circular bulge configurations. Kinematics and force equilibrium will be used to account for geometrically nonlinear effects and to provide relations that convert pressure and center-point displacement, which are measurable parameters, to the stress and strain in the film during deformation. The case of an initially flat film will be considered first, followed by the case of a film with a non-flat initial kinematic state. Lastly, a discussion on how this information can be used to characterize the elastic and viscoelastic constitutive behavior of materials is presented.

2.1 Plane-Strain Bulge Test

Consider a membrane that is clamped flatly over a rigid substrate with a rectangular orifice and subjected to a transverse pressure as shown in Fig. 2.1. For this loading condition, the stress state in the membrane can be approximated as plane-stress, i.e., $\sigma_1 \neq \sigma_2 \neq 0$ and it is assumed that σ_3 is negligible compared to the in-plane stresses. It has been shown previously that a plane-strain condition exists in the $x_1 - x_3$ plane if the longer of the in-plane orifice dimensions is at least four times the length of the shorter dimension (i.e., if $a \leq 4b$) [37, 41]. In this case, the strain in the x_2-direction is zero. For the plane-strain bulge test, an analytical formulation can be derived for the strain in x_1-direction based solely on kinematics by assuming that the deformed shape has a circular cross section [41]. The stress and strain is then uniform in the deformed configuration along the radial direction and can be obtained independently of the constitutive behavior of the material,

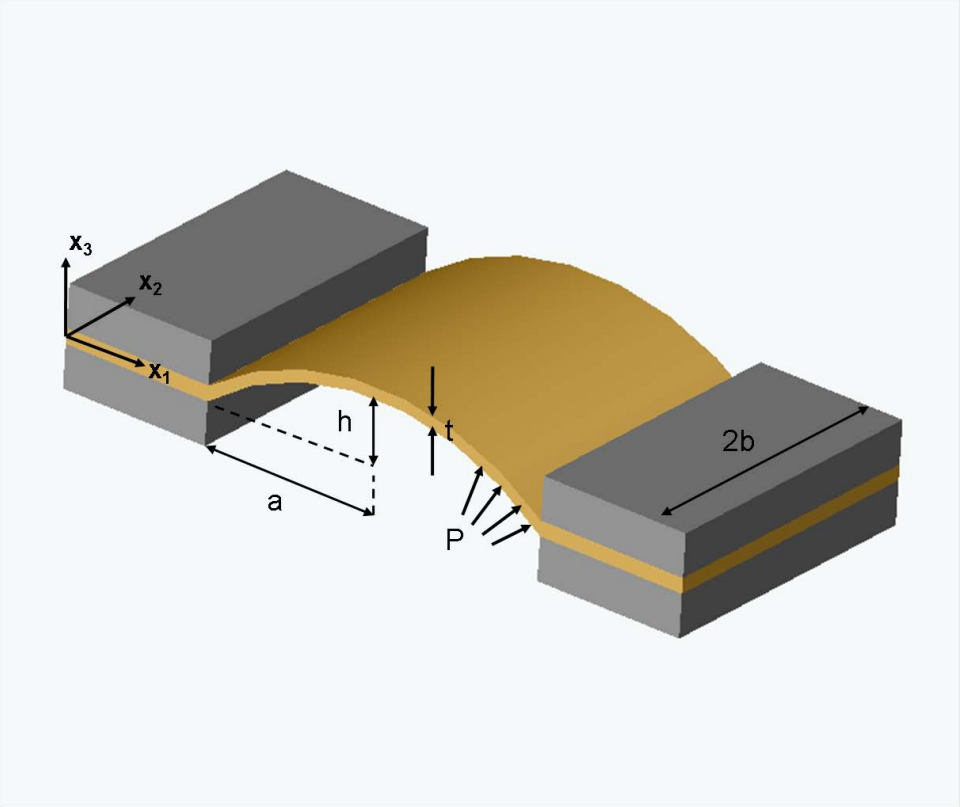

Figure 2.1: Schematic of the plane-strain bulge test

allowing for large deformation and plasticity analysis [41]. The stress is calculated based on the thin-walled approximation of a cylindrical membrane under transverse pressure which is well known and is given as

$$\sigma_1 = \frac{PR}{t}, \tag{2.1}$$

where σ_1 is the nominal stress in the x_1-direction, R is the radius of curvature of the membrane, and t is the thickness of the membrane. Since the radius of curvature is a function of the center-point displacement, h, it becomes necessary to parameterize R in terms of h and a, the latter being the membrane half-length prior to loading. Referring to Figure 2.2, this relationship can be easily found from geometric consideration, and is given as

$$R = \frac{a^2 + h^2}{2h}. \tag{2.2}$$

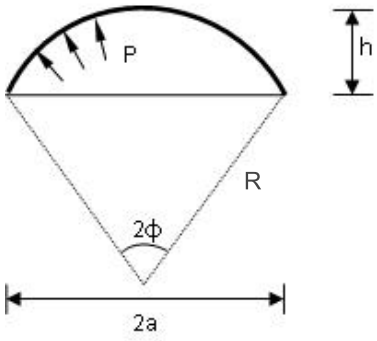

Figure 2.2: Schematic of a cylindrical membrane cross section along the x_1-direction (figure not drawn to scale)

Inserting (2.2) into (2.1) provides the formulation for the stress as a function of the the center-point displacement, h, and the applied pressure, P, in addition to the geometrical constants a and t. This stress relation is given in (2.3) [41] as

$$\sigma_1 = \frac{P(a^2 + h^2)}{2ht}. \tag{2.3}$$

The expression for the nominal strain in the x_1-direction is determined from the change in length of the membrane from its undeformed to deformed configurations divided by the undeformed length. The undeformed length of the membrane is given simply as $2a$. The deformed arc length, s_1, is derived geometrically in (2.4) as

$$s_1 = 2\phi R = 2Rsin^{-1}(\frac{a}{R}) = \frac{a^2 + h^2}{h} sin^{-1}(\frac{2ah}{a^2 + h^2}). \tag{2.4}$$

An expression for the nominal strain is then straightforward and is given below as a function of the center-point deflection, h, and the constant a [41] as

$$\epsilon_1 = \frac{s_1 - 2a}{2a} = \frac{a^2 + h^2}{2ah} sin^{-1}(\frac{2ah}{a^2 + h^2}). \tag{2.5}$$

It is of interest to note here that many researchers who are solely interested in small-strain behavior, reduce (2.3) and (2.5) to a more simple form by enforcing the condition, $h \ll a$. In this case the above stress and strain equations reduce to [41],

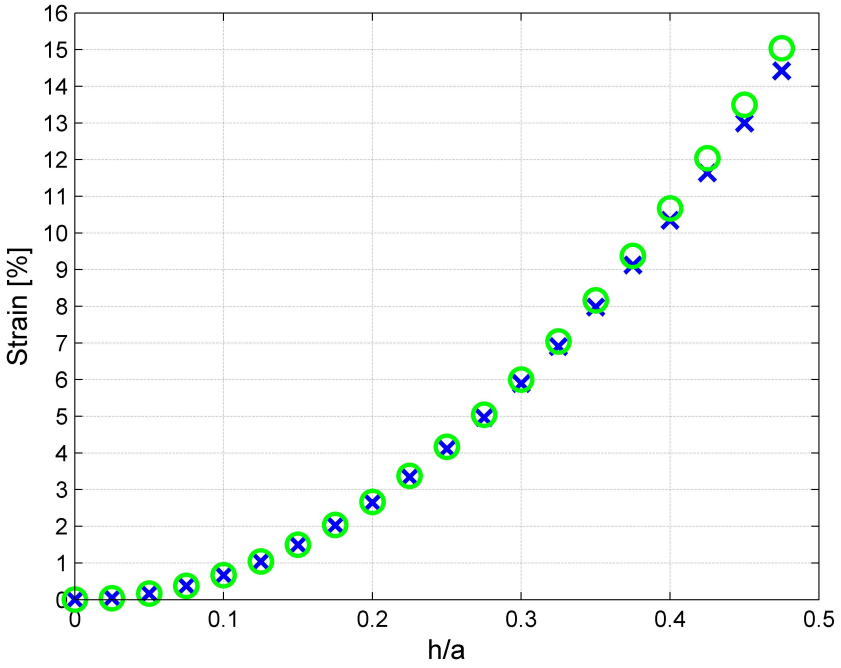

Figure 2.3: Comparison of (2.5) shown with blue crosses and (2.7) with green circles for evaluation of strain (ϵ_1) as a function of h/a

$$\sigma_1 = \frac{Pa^2}{2ht}, \tag{2.6}$$

$$\epsilon_1 = \frac{2h^2}{3a^2}. \tag{2.7}$$

Figure 2.3 shows a plot of (2.5) and (2.7) versus the non-dimensional ratio h/a. It can be seen here that for strains greater than approximately 2 - 3%, deviation between the two equations becomes evident. Therefore, for linearly elastic and viscoelastic analyses of material behavior, where deformations must be kept small, use of (2.6) and (2.7) is sufficient. Conversely, (2.3) and (2.5) must be used to study large deformation phenomena.

2.2 Circular Bulge Test

Consider a membrane that is pressurized using a circular orifice, which provides an equi-biaxial state of stress in the film. In cylindrical coordinates (r, θ, z), the result is that the stress in the r and θ directions are equal, i.e., $\sigma_r = \sigma_\theta$, with σ_z approximated as zero for plane-stress. In this case, the stress formulation for a thin-walled membrane under transverse pressure is reduced by a factor of two from the stress given in (2.1) for the plane-strain case. Therefore, the membrane stresses in the biaxial case are known to be [31]

$$\sigma_r = \sigma_\theta = \frac{PR}{2t}. \tag{2.8}$$

The kinematics of the circular bulge problem is the same as the plane-strain case, and so substituting (2.2) into (2.8) provides the stress formulation for the circular bulge test given below as

$$\sigma_r = \sigma_\theta = \frac{P(a^2 + h^2)}{4ht}. \tag{2.9}$$

In this case, the reduced form of the stress formulation (when $h \ll a$) becomes

$$\sigma_r = \sigma_\theta = \frac{Pa^2}{4ht}. \tag{2.10}$$

Again, since the kinematics of the plane-strain and circular bulge configurations are identical, the strain formulation for both of them are the same. So to determine the change in length of an arc along the radial direction (or circumferential expansion, since the strain is also biaxial in the $r - \theta$ plane), (2.5) and/or (2.7) can be used.

2.3 Plane-Strain and Circular Bulge Tests with Initial Non-Zero Deflection

The theory outlined in the previous two sections is based upon two very important assumptions that must hold true experimentally to be used in interpreting measurements. The first is that the center-point displacement, h, must be less than the membrane half-length, a (i.e., $h \leq a$). The second is that the membrane must be initially flat prior to loading, which may be more difficult to achieve depending upon the material tested and whether or not bonding, clamping, or deposition methods are used. Therefore, the case of a membrane with an initial height prior to loading is considered in this section.

The existence of a confinement pressure during film clamping can lead to the film slipping between the plates which makes the initial kinematic state of the film harder to control. As a result, the film may be radially and symmetrically bulged subsequent to clamping and prior to any loading being applied. Hence, we consider a clamped membrane under a confinement pressure, P_0, with a symmetric initial displacement in the radial direction. This state is shown pictorially in Figure 1.3 and the center-point height of this initial kinematic state is labeled h_0.

The undeformed length, s_0, of the membrane arc in the x_1-direction for the plane-strain configuration or the r-direction for the biaxial case can be easily determined from (2.5) to be

$$s_0 = \frac{a^2 + h_0^2}{h_0} sin^{-1}(\frac{2ah_0}{a^2 + h_0^2}). \tag{2.11}$$

The undeformed length given above is taken as the initial position of the membrane at zero strain. Any subsequent deformation will increase the center-point displacement of the membrane by an amount equal to h, and subsequently change the arc length of the film. We must now consider a new parameterization for R that includes the initial center-point height, h_0, which is given as

$$R = \frac{a^2 + (h_0 + h)^2}{2(h_0 + h)}. \tag{2.12}$$

The deformed length, s_1, is thereby given below as

$$s_1 = \frac{a^2 + (h_0 + h)^2}{h_0 + h} sin^{-1}(\frac{2a(h_0 + h)}{a^2 + (h_0 + h)^2}). \tag{2.13}$$

The stretch ratio, λ, can be defined as the ratio between the deformed length, s_1, and the undeformed length, s_0, and is used here in place of nominal strain. For large deformation analysis, the stretch ratio is typically used, however, the strain-stretch relationship is straightforward and well known ($\lambda = \epsilon + 1$). For completeness, the stretch ratio is provided below as

$$\lambda_1 = \lambda_r = \frac{s_1}{s_0}. \tag{2.14}$$

As indicated in the previous section, the equations above, which provide a kinematic description of the stretch in the membrane, applies to both the plane-strain and the circular bulge configurations. We now move to the stress state for the case with an initial film deflection. The effect of the initial (confinement) pressure, P_0, must be subtracted from the stress formulation to enforce a zero stress state before loading. Otherwise, one would erroneously find an "apparent residual stress" in the membrane. As mentioned in Chapter 1, many researchers are interested in the determination of residual stress for films deposited onto substrates, however, the admission of a deflection profile in the undeformed configuration renders the effects of residual stress incalculable. Following directly from (2.3), the stress relation for the plane-strain case is

$$\sigma_1 = \frac{(P - P_0)[a^2 + (h_0 + h)^2]}{2(h_0 + h)t}, \tag{2.15}$$

and for the circular configuration,

$$\sigma_r = \sigma_\theta = \frac{(P - P_0)[a^2 + (h_0 + h)^2]}{4(h_0 + h)t}. \tag{2.16}$$

Again, here we will switch convention to use the true (Cauchy) stress, which takes account of the change in cross-sectional area as a material undergoes large stretching. The true stress relations for

both the plane-strain and circular configurations are provided in (2.17) and (2.18) as

$$\Sigma_1 = \sigma_1 \lambda_1 = \frac{(P - P_0)[a^2 + (h_0 + h)^2]}{2(h_0 + h)t} \lambda_1, \tag{2.17}$$

$$\Sigma_r = \sigma_r \lambda_r = \frac{(P - P_0)[a^2 + (h_0 + h)^2]}{4(h_0 + h)t} \lambda_r. \tag{2.18}$$

Figures 2.4 and 2.5 show plots of stretch vs. center-point displacement for the case of a flat membrane and for a membrane with initial radial deflections having center-point heights of 1 mm, 2 mm, 3 mm, and 4 mm. Here, the membrane half-length, a, is taken to be 7.5 mm, and Figure 2.4 shows a clear deviation in the stretch calculation depending upon the initial kinematic state of the membrane. As shown in these figures, the geometric nonlinearity of the problem necessitates the measurement of center-point height for initially non-flat membranes, even if h_0 is as small as 6% of the orifice length, $2a$.

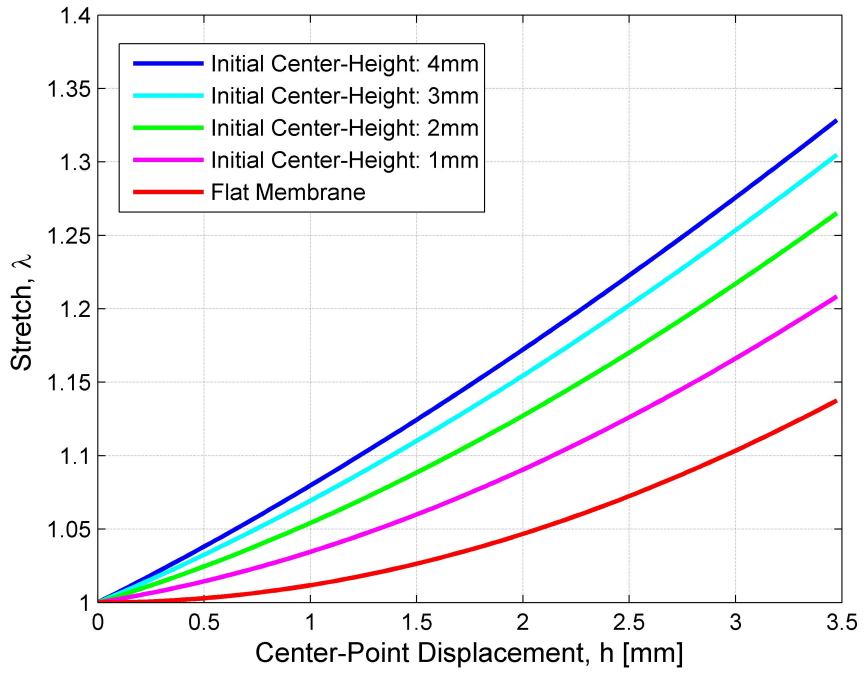

Figure 2.4: The effect of initial film deflection on stretch determination at large deflections ($h \approx a$) for a cylindrically bulged membrane

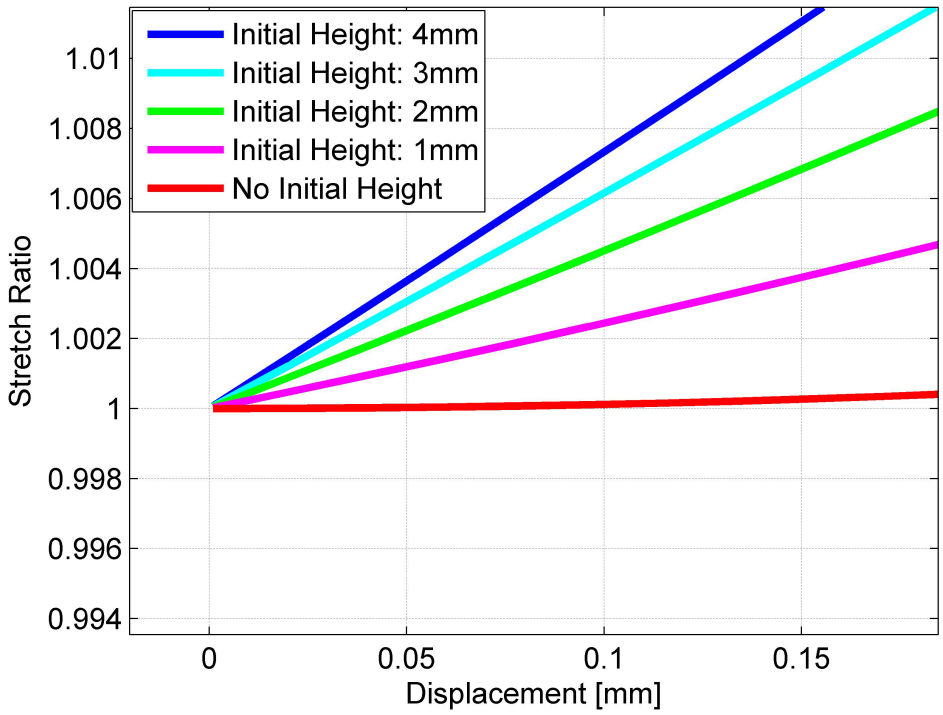

Figure 2.5: The effect of initial film height on stretch determination at small deflections ($h \ll a$) for a cylindrically bulged membrane

2.4 Determination of Elastic Constants

As stated in the previous chapter, the bulge test has been used extensively as a characterization tool for determining the constitutive properties of thin-film materials. Regardless of the configuration chosen, the bulge test is intrinsically unable to deconvolve the Young's modulus, E, and Poisson's ratio, ν, of a material. However, one can independently determine E and ν of a material by conducting the plane-strain and circular bulge tests in tandem [37]. This section elucidates the method by which one could use these pressure-displacement techniques to determine the elastic properties of a bulk membrane material.

For a membrane pressurized using the plane-strain configuration, the stress and strain states are

$$\sigma_{ij} = \begin{pmatrix} \sigma_1 & 0 & 0 \\ 0 & \sigma_2 & 0 \\ 0 & 0 & 0 \end{pmatrix}, \tag{2.19}$$

and

$$\epsilon_{ij} = \begin{pmatrix} \epsilon_1 & 0 & 0 \\ 0 & 0 & 0 \\ 0 & 0 & \epsilon_3 \end{pmatrix}. \tag{2.20}$$

We now seek a relationship between σ_1 and ϵ_1 using Hooke's law for a homogeneous, linearly elastic, and isotropic solid, which is

$$\epsilon_{ij} = \frac{1}{E}[(1+\nu)\sigma_{ij} - \nu\sigma_{kk}\delta_{ij}]. \tag{2.21}$$

Evaluating Hooke's law for the stress and strain given above provides the relations

$$\epsilon_1 = \frac{1}{E}(\sigma_1 - \nu\sigma_2) \tag{2.22}$$

and

$$\epsilon_2 = \frac{1}{E}(\sigma_2 - \nu\sigma_1) = 0. \tag{2.23}$$

Solving these equations provides the relationship needed between σ_1 and ϵ_1:

$$\sigma_1 = \frac{E}{1-\nu^2}\epsilon_1 = M\epsilon_1, \tag{2.24}$$

where the expression $E/(1-\nu^2)$ is denoted as the plane-strain modulus of a material, and hereafter is referred to by the letter M.

Next, for a membrane pressurized using the circular configuration, the stress and strain states are as follows:

$$\sigma_{ij} = \begin{pmatrix} \sigma & 0 & 0 \\ 0 & \sigma & 0 \\ 0 & 0 & 0 \end{pmatrix}, \tag{2.25}$$

$$\epsilon_{ij} = \begin{pmatrix} \epsilon & 0 & 0 \\ 0 & \epsilon & 0 \\ 0 & 0 & \epsilon_3 \end{pmatrix}. \tag{2.26}$$

Again applying Hooke's law, it is straightforward to determine the relationship between σ and ϵ for the biaxial case to be

$$\sigma = \frac{E}{1-\nu}\epsilon = B\epsilon, \tag{2.27}$$

where the expression $E/(1-\nu)$ is denoted as the biaxial modulus of a material, and hereafter is denoted by the letter B.

It is now clear that the two tests (plane-strain and circular) can be used together to evaluate E and ν for a specific material. Finally, the following empirical relations in (2.28) and (2.29) can be used to extract the elastic constants once M and B are determined from experiments. These relations are

$$E = 2B - \frac{B^2}{M} \tag{2.28}$$

and

$$\nu = \frac{B}{M} - 1. \tag{2.29}$$

2.5 Viscoelastic Analysis in the Time and Frequency Domains

It is well known that viscoelastic analysis can be conducted on a material in either the time or frequency domains. In the time domain, measurements are usually conducted by applying a fast ramp increase in strain (to simulate instantaneous loading) and monitoring changes in stress over time, referred to as stress relaxation. Conversely, a fast ramp increase in stress could be applied with the strain being monitored in time, which is referred to as a creep test. Results from such tests allow researchers to determine both the instantaneous and equilibrium behaviors of time-dependent materials.

Consider a stress relaxation test conducted on a linearly viscoelastic material using a circular (spherical) bulge configuration. In this case a step increase in strain, denoted as ϵ_0, would cause a time-dependent decrease in stress, which we denote as $\sigma(t)$. Using (2.27), we can define the biaxial relaxation modulus, $B(t)$, as

$$B(t) = \frac{\sigma(t)}{\epsilon_0} = \frac{E(t)}{1-\nu}. \tag{2.30}$$

This result holds without regard to whether or not the membrane is initially flat since $\sigma(t)$ must be calculated using the relations presented previously.

In contrast to viscoelastic analysis in the time domain, viscoelastic analysis in the frequency domain is conducted by applying an oscillatory loading profile in time over a wide range of frequencies. This method also allows for the characterization of time-dependent materials, but in a slightly different manner. If strain is controlled in an oscillatory loading configuration, then a measured stress profile would have the same frequency but would display a phase lag with respect to the strain profile in time [9, 27, 12]. This phase lag is due to viscoelastic behavior and is used to quantify the viscous and elastic nature of such materials. The following analysis shows how the bulge test could be used to conduct such an experiment for the case of an initially flat membrane.

Let us consider the circular (spherical) bulge configuration and introduce an oscillatory pressure

profile in time, $P(t)$, of the form,

$$P(t) = |P|\, e^{i\omega t}, \tag{2.31}$$

where $|P|$ is the amplitude of pressure, ω is the angular frequency of oscillation, and t denotes the time variable.

If the material exhibits linearly viscoelastic behavior, the center-point displacement profile in time, $h(t)$, would have the form below:

$$h(t) = |h|\, e^{i\omega t - \delta}, \tag{2.32}$$

where $|h|$ is the amplitude of the displacement and δ is the measured phase angle difference between the displacement and pressure profiles. Inserting these time-dependent profiles into (2.10) provides a relation for the complex stress amplitude, σ^*, which is given as

$$\sigma^* = \frac{a^2}{4t}\frac{|P|}{|h|}e^{i\delta}. \tag{2.33}$$

Determining the amplitude of strain, $|\epsilon|$, (using (2.7)) yields

$$|\epsilon| = \frac{2\,|h|^2}{3a^2}. \tag{2.34}$$

Dividing (2.33) by (2.34) provides a relation for the complex biaxial modulus, B^*:

$$B^* = \frac{\sigma^*}{|\epsilon|} = \frac{3a^4\,|P|}{8t\,|h|^3}e^{i\delta} = \frac{E^*}{1-\nu}, \tag{2.35}$$

where E^* is the complex modulus in tension. It is important to note here, that ν could very well be a function of frequency and is not necessarily a time-independent quantity, however for simplicity we will assume it to be constant as there is no direct way to determine it using time-dependent results from the bulge test.

At this point we define the storage and loss biaxial moduli of a material tested using the circular

configuration, which we will denote as $B^{'}$ and $B^{''}$ respectively. The storage and loss moduli are frequency-dependent viscoelastic functions, and the latter is used to quantify the viscous dissipation of energy during cyclic loading [9, 27, 12]. The mathematical definition of $B^{'}$ and $B^{''}$ is given in (2.36) as

$$B^{*} = \frac{3a^{4}\left|P\right|}{8t\left|h\right|^{3}}(cos\delta + isin\delta) = B^{'} + iB^{''} = \left|B^{*}\right| e^{i\delta}. \tag{2.36}$$

Lastly, we will provide a relation for the loss tangent, $tan\delta$, which is a ratio of the loss modulus to the storage modulus. The loss tangent also quantifies the mechanical loss in a viscoelastic material due to the viscous dissipation of energy [9, 27, 12] and is known to be

$$tan\delta = \frac{B^{''}}{B^{'}}. \tag{2.37}$$

Of the four parameters derived above–complex modulus, loss modulus, storage modulus, and loss tangent–only two of them are independent. The extension of the aforementioned viscoelastic analysis to the case of an initial film deflection is a straightforward task and can be achieved by considering the analysis in Section 2.3 combined with the time-dependent analysis in this section. Finally, the viscoelastic result for the case of the plane-strain (cylindrical) bulge configuration is given below as

$$M^{*} = \frac{3a^{4}\left|P\right|}{4t\left|h\right|^{3}}e^{i\delta} = \frac{E^{*}}{1-\nu^{2}}, \tag{2.38}$$

and

$$M^{*} = \frac{3a^{4}\left|P\right|}{4t\left|h\right|^{3}}(cos\delta + isin\delta) = M^{'} + iM^{''} = \left|M^{*}\right| e^{i\delta}, \tag{2.39}$$

where M^{*}, $M^{'}$, and $M^{''}$ are the complex plane-strain modulus and plane-strain storage and loss moduli, respectively.

The above analysis is presented for an initially flat membrane. In the case where there exist a

non-zero initial deflection of the membrane, one would calculate the stresses and strains using the relations presented in Section 2.3. Then the amplitudes of strain and stress, $|\epsilon|$ and σ^*, respectively, can be determined directly from strain and stress vs. time profiles using fits to the data.

2.6 Geometric Conditions for Membrane Behavior

So far, we have discussed the mechanics of a membrane under transverse pressure loading using the plane-strain and circular configurations. However, we have not explored the geometric requirements for membrane behavior. Ventsel and Krauthammer proposed that a membrane is distinct from a thin plate in that their ratios of $2a/t$ are in the range of $80 - 100$ or above, whereas a plate would be classified by having a ratio of $2a/t \leq 80$ [36]. Both Kirchhoff's theory of thin plates and the membrane theory reviewed above assume the condition of plane-stress in the $x_1 - x_2$ plane. However, Kirchhoff's plate theory assumes that the applied load is carried only by bending moments and shear forces, and therefore axial stretching due to membrane forces is neglected [36]. Though, in the case of an extensible plate, both membrane forces and contributions due to flexural forces are considered [36]. Also, membrane analysis neglects edge effects and looks at the material behavior far from the boundary, while plate theory is heavily dependent upon the boundary conditions. All of this implies that in the vicinity of a certain aspect ratio, there exists a transition from extensible plate behavior to membrane behavior.

Using the commercially available finite element software package, ABAQUS, we sought to evaluate the supposition proposed by Ventsel and Krauthammer by simulating the pressure-bulge technique for various values of the aspect ratio, $2a/t$. This was done by increasing the thickness of the material while the orifice geometry was held constant at $2a = 15\ mm$. In this sense, the data presented from the simulations are functions of varying thickness and not changes in the in-plane dimensions. As shown in Figure 2.6, symmetry conditions were enforced along the free edges, so that only one-fourth of the membrane needed to be modeled using the plane-strain bulge configuration. Additionally, along the clamped boundary displacements were restricted in all directions. The ABAQUS element type, C3D8R (an 8-node linear brick element with reduced integration and hour-

glass control) was used with 4500 total elements for all of the simulations, except for the simulation in which $2a/t = 7.5$, which had 9000 elements. An elastic material model was used with $E = 51$ kPa and $\nu = 0.45$ (nearly incompressible). The simulations were run for aspect ratios of 7.5, 15, 30, 60, 75, and 100, which correspond to thicknesses of 2, 1, 0.5, 0.25, 0.2, and 0.1 mm, respectively.

Figure 2.7 shows the non-dimensional stress parameter, σ_1/P, as a function of position along the x_1-direction for the top and bottom surfaces of the plate (the location $x/a = 0$ is the clamped boundary and $x/a = 1$ is the membrane center-point). It can be clearly seen that as the aspect ratio changes there exist a clear deviation in the stress behavior, especially away from the boundary. As expected, for $2a/t = 7.5$, there is a neutral axis (zero stress) in the plate, which is consistent with pure bending theory. As the aspect ratio increases, however, the emergence of membrane stresses appear as indicated by the tendency of the normalized stress (stress / applied pressure) toward higher values away from the boundary. Close to the boundary, the bottom of the plate/membrane is in a state of tension and and the top is in a state of compression for each geometry. However, farther away from the boundary the stress in the bottom of the membrane becomes greater than the stress in the top, indicating in each case a transition in stress at a certain value of x/a. The distance from the boundary to these discrete points of transition is referred to as the boundary layer. Boundary layer analysis gives an indication as to how far bending effects due to clamping propagate through the material. It can be seen in the figures that as the thickness decreases, the points at which these transitions happen are closer toward the boundary, implying a decreasing boundary layer. This result is consistent with membrane theory. Figure 2.8 shows the same information but for the two highest aspect ratios. Is is seen that the behavior of these two aspect ratios is markedly different from those in Figure 2.7. The most notable change is the relatively little difference between stresses plotted along the top and bottom surfaces. Again this result is consistent with membrane theory as the membrane stresses do not vary throughout the thickness. Lastly, as seen in Figure 2.8 the stresses in the center of the membrane are less than the stresses near the boundary. The effect of non-uniformity in the in-plane stresses was also observed by Small and Nix [31] for their analysis of membrane behavior using finite element modeling. These simulations agree well with the

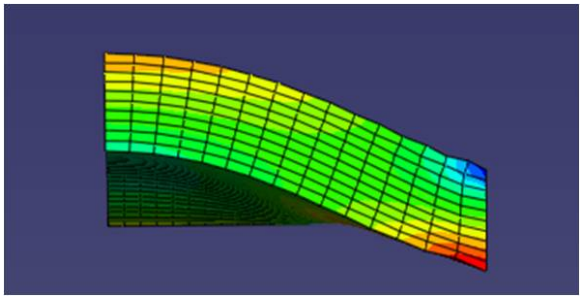

(a) $2a/t = 7.5$

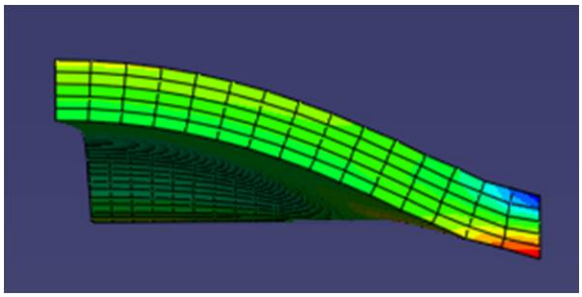

(b) $2a/t = 15$

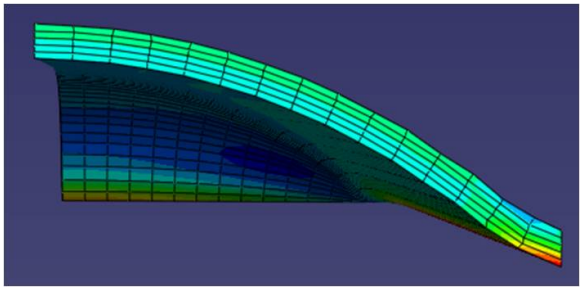

(c) $2a/t = 30$

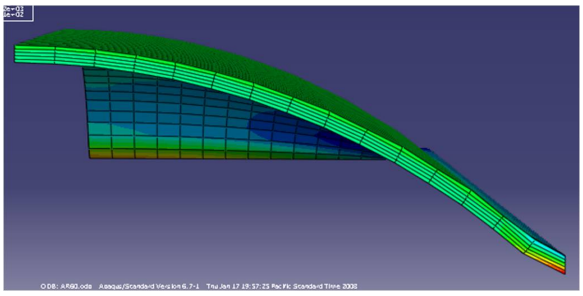

(d) $2a/t = 60$

Figure 2.6: Stress contours of Σ_1 shown in the deformed configuration for simulations at various aspect ratios of $2a/t$. Red corresponds to areas of highest tensile stress while dark blue corresponds to areas of highest compressive stress. The scale is not the same for each figure.

supposition proposed by Ventsel and Krauthammer that membrane behavior can be observed for in-plane length to thickness ratios, $2a/t$, in the range of 80 and greater.

2.7 Conclusions

The equations and analysis presented above allow for the interpretation of experimental data using the pressure-bulge technique. The large deformation equations presented in this chapter will be used to interpret results obtained for latex and silicone, which are presented in Chapter 4. The viscoelastic analysis will likewise be used in the interpretation of the results on the agarose gels presented in Chapter 5. The parametric study using ABAQUS was conducted to determine the minimum aspect ratio that could be used in the experiments to obtain accurate and reliable data. Because no full-field displacement measuring technique is used here, as in some of the more conventional setups, there needs to exist an *a priori* knowledge that the kinematic assumptions upon which the theory above is based are not violated in the experiments. Therefore, the geometry must be such that deformation occurs in the membrane regime. While this is not a huge issue for commercially available materials that are sold in an array of thicknesses, such as the synthetic polymers used in the study, for the agarose gels the issue of forming them into sheets becomes extremely difficult as you attempt to decrease the thickness. Therefore, there is a trade off between the in-plane geometries and the thickness of samples that must be carefully examined prior to testing.

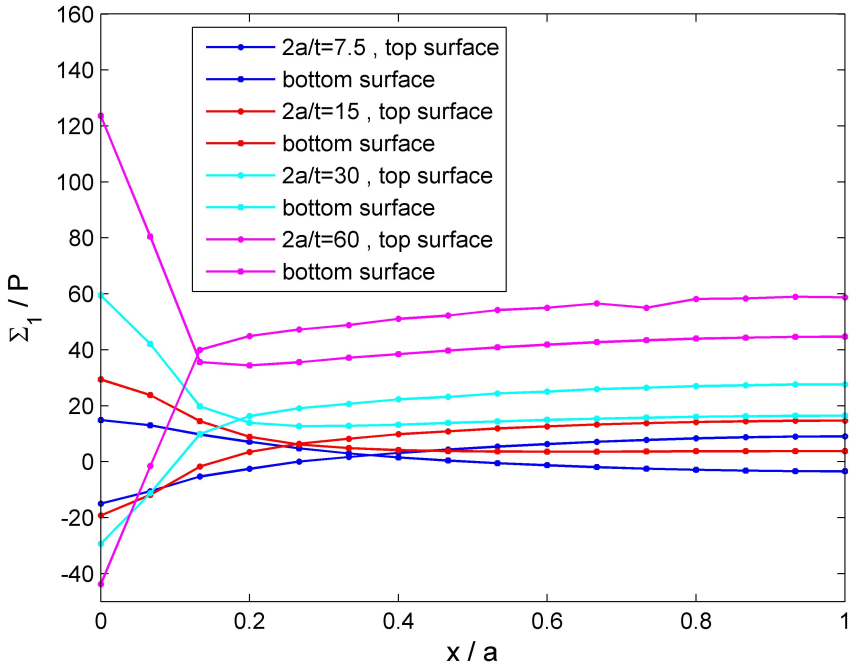

Figure 2.7: Stress normalized by pressure as a function of position along the x_1-direction obtained for simulations for various aspect ratios in the plate regime

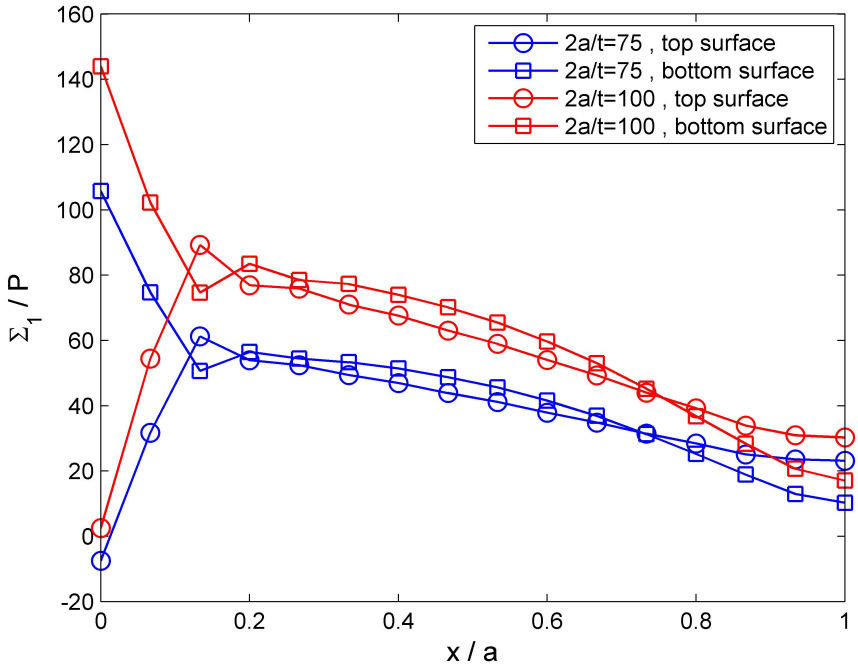

Figure 2.8: Stress normalized by pressure as a function of position along the x_1-direction obtained from simulations for two aspect ratios in the membrane regime

Chapter 3

Experimental Setup

The experimental setup used to perform the pressure-bulge experiments is shown schematically in Fig. 3.1. This setup has four main components: a pressure chamber, a motor-driven syringe, a pressure sensor, and a displacement sensor. In addition, the control and data collection hardware and software include use of a digital multimeter, a controller for the displacement sensor, and an analog-to-digital (A/D) board and PCI card interfaced with LabVIEW software (National Instruments, Austin, TX, USA). A picture of this setup is also provided in Figure 3.2.

The liquid pressure chamber is made of stainless steel and is designed such that two plates with orifices of arbitrary dimensions are fixed to the chamber with screws as shown in Figure 3.3. The polymeric samples are clamped between the two stainless steel plates and brought into contact with the water in the chamber as shown in Figure 3.4. Two threaded holes are drilled into the sides of the chamber so that the pressure sensor is connected on one side and the other side is connected to the syringe via a pipe fitting. The plates have thicknesses of 0.25 in (6.35 mm) and the orifice dimensions used in these experiments is a 15 x 61 mm^2 rectangular orifice and two circular orifices of 1 in (25.4 mm) and 1.5 in (38.1 mm) diameters.

The pressure in the chamber is altered by the reciprocal motion of the syringe, which is connected to a miniature linear actuator (Model # LC25, Bearing Engineers, Aliso Viejo, CA, USA). This linear actuator has a stroke length of 116 mm, a screw lead of 0.25 in/rev, and static and dynamic load capabilities of 240 N and 213 N, respectively. The actuator is controlled by a rotary motor (Model # 1715, Intelligent Motion Systems, Marlborough, CT, USA) that has a 120 V AC power supply

(Model # IP402, Intelligent Motion Systems). This motor is a 200 full-step motor (200 steps/rev), but has microstepping capabilities up to 51200 microsteps/rev. This translates to a 124 nm step size for the linear actuator, when the motor is set to the smallest step increment, which is typically used as default. Also, the motor torque decreases with increasing speed, and at the highest speed of 7000 full steps/s, this value is 11 N·cm. The axial force capability of the actuator can be estimated using the relation: Force = (Torque $\times$ 2π $\times$ Efficiency)$\div$ Lead. The manufacturer suggested that the motor efficiency lies in the range of 0.5 to 0.6. Using 0.5 as the motor efficiency and the lowest possible value for motor torque, 11 N·cm, the axial force capability is estimated to be a minimum value of 54.4 N. This force capability is more than sufficient for the class of materials studied in this investigation.

As the pressure is varied in the chamber, the pressure sensor (Model # PX01-CO, Omega Engineering, Stamford, CT, USA) monitors these changes in real-time. This sensor measures gage pressure and has a measuring range of 0 - 5 psi (0 -3 4.474 kPa) with an accuracy of 0.0025 psi (17.237 Pa). However, the typical pressures in these investigations fluctuate from a hydrostatic pressure of about 1.62 psi (11.169 kPa) to about 3 psi (20.684 kPa), which is limited by the imposed stroke. The pressure sensor has a 4 to 20 mA current output and is powered and controlled by a digital multimeter (Model # DP41-B, Omega Engineering). The multimeter reads the sensor value and sends a 0 - 10 V analog signal to the A/D data acquisition card (Model # DP41-B PCI-6221 and BNC 2120 accessory, National Instruments). The digital multimeter has six A/D conversion rates in the range of 5.7 - 134.9 ms, and as conversion rate increases the accuracy of the measurement is diminished. The fastest conversion rate used for the experiments in this study was 18.2 ms.

The center-point displacement of the specimen is measured using a confocal chromatic displacement sensor (Model # 2400, Micro-Epsilon, Ortenburg, Germany). This sensor is particularly suited for samples with high light transparency, as it takes advantage of the chromatic deviation of white light focused through a multi-lens arrangement as shown in Figure 3.5. This feature increases the sensitivity of the sensor and allows for 0.4 μm displacement resolution over a range of 10 mm. The displacement sensor has a controller which operates in two main modes: distance and thickness.

The distance mode provides the distance from the sensor head to the first surface in the measuring range. Alternatively, the thickness mode provides the distance in between two surfaces where both must lie in the measuring range, and the medium between the two surfaces must be optically homogeneous and transparent with a known refractive index. The thickness mode was used in this study to track the center-point displacement of the samples through a thin water layer on top of the samples, thus allowing for fully hydrated experiments in cases where this was required, however, it should be noted that testing in this way decreased the resolution of the measurements to about 10 μm. The controller comes with its own display and control software via a RS-232 serial interface, but instead the two-channel analog output option was used, by sending a 0 - 10 V signal to the A/D card. The confocal displacement head is mounted above the pressure chamber and connected to a bi-directional linear guide that is hand-controlled. The center-point location of the membrane was first determined by visual estimation for each plate geometry used, and once that position was determined the displacement sensor and bulge chamber were held in place for consistency throughout the measurements.

Using the LabVIEW software, the pressure and displacement signals are collected in real time. Because the control software for the motor is not compatible with LabVIEW, a separate control software was used to operate the motor, which was provided by the manufacturer. As a result, an external trigger was used to start all of the measurements. The LabVIEW program and external trigger allowed for time synchronization of the data from the digital multimeter and the displacement sensor controller, and, using the program, the number of samples and sampling times for the experiments were controlled directly. Post-processing of data was carried out using MATLAB software (Mathworks, Natick, MA, USA). Finally, as shown in the picture of the setup, all measurements were performed on a vibration isolated table to reduce errors due to vibrations.

There are several sources of error attributed to this type of test, and additional sources of error are propagated due to the types of materials tested in this study. The most pronounced source of error is the inaccurate determination of the initial film state and measurement of the initial film height. Accurate measurement of initial height is straightforward in the case of an elastic

material, but for a viscoelastic material, relaxation occurs in the material due to clamping, and therefore the initial height does not remain constant prior to starting the measurements. As a result, the viscoelastic samples were clamped and allowed to come to an equilibrium position before the measurement of the initial height and the start of each experiment. Another source of error is in the determination of the center-point displacement by visual estimation and use of a single-point displacement measurement. While this did not appear to have any drastic effects on the data, not having a full-field displacement measuring technique does require some conditions to be assumed instead of determined, such as the assumption of a spherical geometry in the initial kinematic film state. Using a single-point measurement with scanning capabilities could help with this issue, but that would require the use of an automated bi-directional linear guide to connect to the confocal sensor head. Since the guide used here was hand controlled, scanning across the sample was not possible since the out-of-plane measurement is altered during the scan due to disturbances applied by the user. Other sources of error are intrinsic to the bulge test and include film slipping and boundary effects. Sample slip at the boundary was prevented for all of the samples by placing an O-ring around the periphery of the orifice in each plate. The O-ring provided a pressure seal that prevented the samples from slipping and rotating after clamping. Also, as mentioned in the previous chapters, boundary effects can seriously decrease the accuracy of results obtained under the membrane assumption. While one could design a bulge configuration in which the in-plane to thickness ratios are well in excess of 100, this option is not feasible for the specimen geometries used in the study. For example, for a specimen thickness of 0.5 mm, an in-plane geometry of 50 mm would be needed to achieve an aspect ratio of 100. And if one wanted to used a plane-strain configuration for this thickness, then this would require the larger rectangular dimension to be at least 200 mm. Given these laboratory constraints, the assumption of uniformity of stress and strain is usually violated depending on material compliance and sample geometry. In this study, geometries were used that minimize the boundary effects and while these effects were not investigated directly by experimentation, all data was compared with data obtained from uniaxial tension tests to determine accuracy.

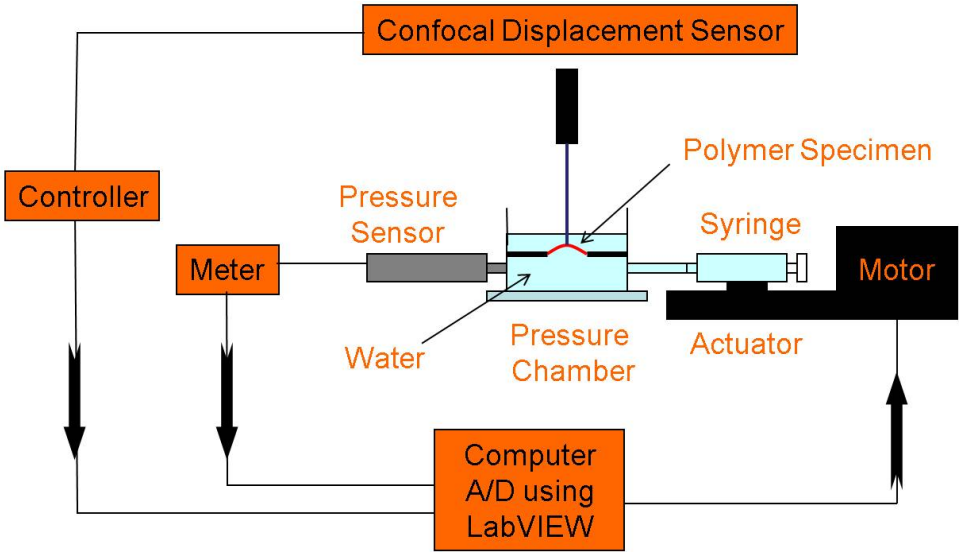

Figure 3.1: Illustrative overview of the pressure-bulge experimental setup for evaluating the elastic and time-dependent behavior of soft polymers and gels

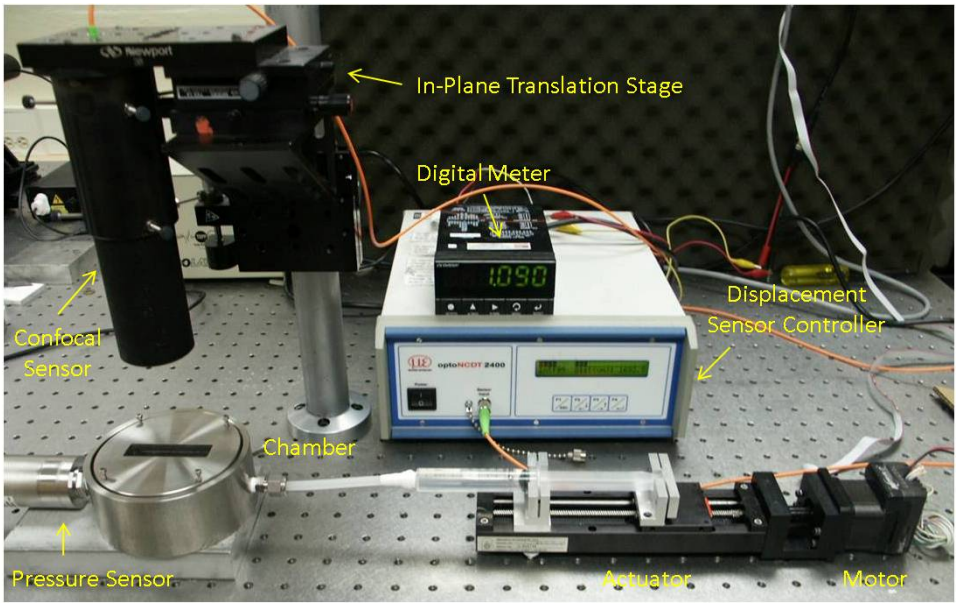

Figure 3.2: Photograph of the pressure-bulge experimental apparatus

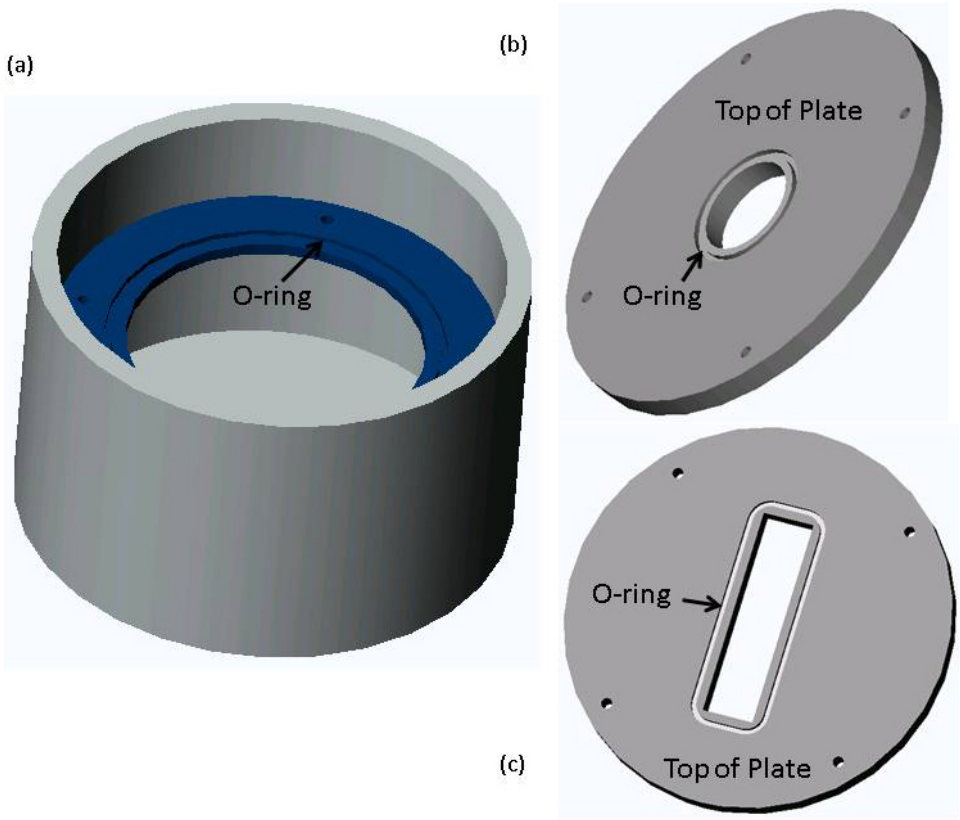

Figure 3.3: (a) Schematic of the pressure chamber used in this study. (b) and (c) Stainless steel clamping plates made with a circular and a rectangular orifice, respectively

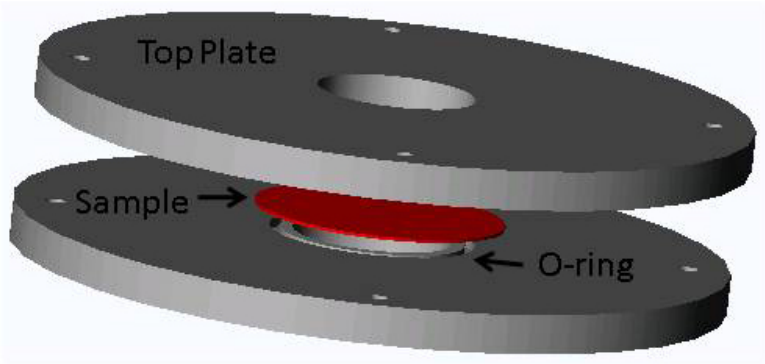

Figure 3.4: Schematic detailing the clamping process of a polymer specimen between two stainless steel plates

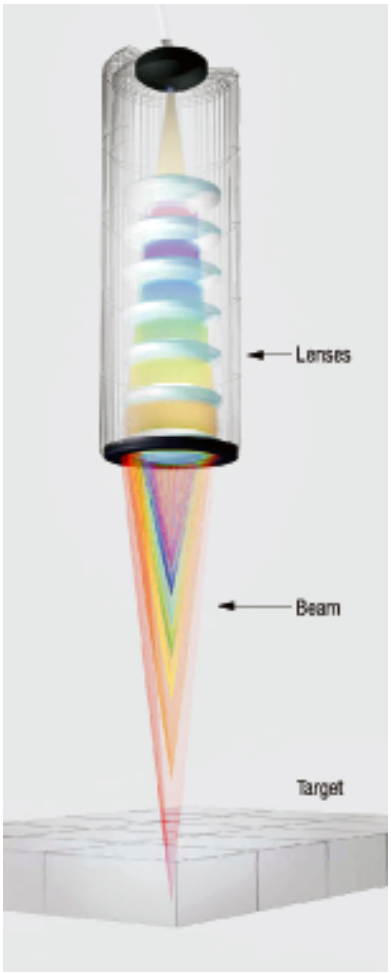

Figure 3.5: Schematic of the confocal displacement measuring principle, which shows the multi-lens arrangement used to focus polycromatic light onto a transparent target (from Micro-Epsilon, Ortenburg, Germany)

Chapter 4

Characterization of Rubber Elastomers

4.1 Materials and Methods

The synthetic polymers tested in this study are commercially available latex and silicone rubber sheets with 100 μm thicknesses. The latex rubber is 97% natural latex and was obtained from McMaster Carr (Los Angeles, CA, USA), while the silicone rubber sheets were fabricated at Specialty Silicone Fabricators (Paso Robles, CA, USA). Rubber elastomers are typically formed through vulcanization and that process involves the addition of fillers (often carbon black) used to increase the tensile strength and maximum elongation of the native material [5]. This is what gives elastomers their hypereastic behavior, and the process is believed to cause the stress-softening and/or viscoelastic effects observed for some elastomers [5]. It is not clear what fillers are used in the production of these rubbers, and in the case of silicone, it is not clear what percentage of the material is natural silicone. However, both materials were chosen because of their low elastic moduli, high elastic range, and nearly incompressible behavior. Because the behavior of incompressible rubbers is well known, these materials serve as good models to determine the viability of the experimental facility.

It has been known for some time that there are deviations in the mechanical behavior of certain polymers tested under dry conditions vs. in the presence of moisture. The typical stress-strain behavior of latex and silicone rubber tested in tension under fully hydrated and dry conditions are shown in Figures 4.1 and 4.2. For latex, a clear difference is seen from the onset of loading,

highlighting the significant effects of moisture on material properties. As seen in the figure, hydration softens the latex and reduces its Young's modulus by about 27%. In the case of silicone, the deviation in the low strain regime is small; however as the strain increases the softening effects due to hydration become more evident. As a result, any mechanical characterization of the rubbers used in this study must be done under consistent moisture conditions to ensure repeatable measurements.

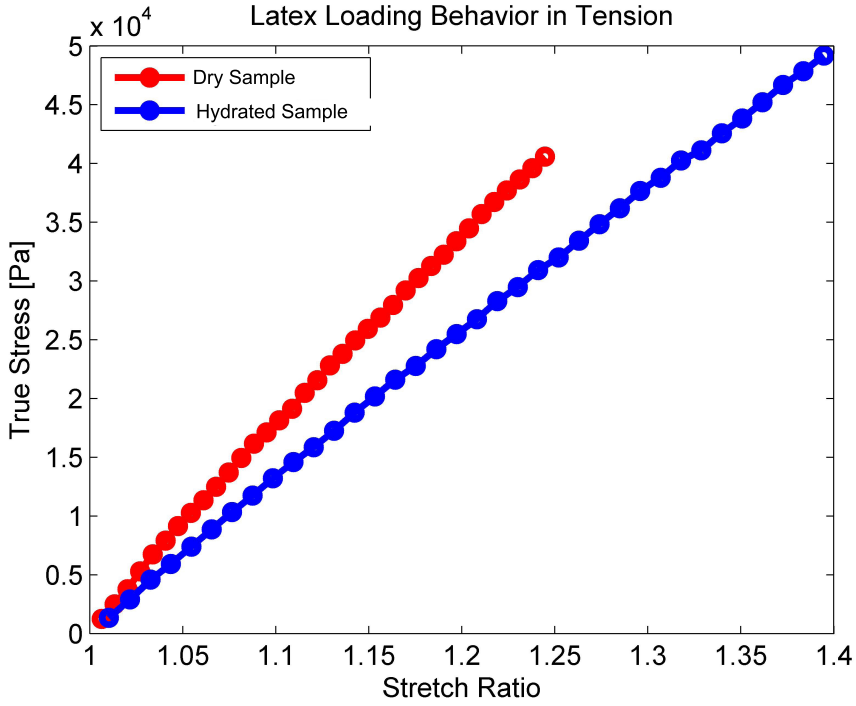

Figure 4.1: Loading behavior of latex in tension under dry and hydrated conditions

Both the latex and silicone rubber sheets were cut and clamped between two stainless steel plates as show in Figure 3.4. The latex and silicone sheets used in the plane-strain bulge test were cut into dimensions of 25 x 71 mm^2 or greater and the latex sheets used in the circular bulge test were cut into 36 x 36 mm^2 or greater squares. This was to ensure that the samples were pressed over the O-ring to limit slipping and rotations around the boundary. Additionally, water-resistant and double-sided tape was used to stretch the membrane across the orifice as flatly as possible. The sample was then sandwiched in the middle of the two plates and screwed into the chamber as shown in Figure 3.3. As mentioned previously in Chapter 2, Section 2.3, the existence of a confinement pressure upon clamping increases the difficulty in controlling the initial deflection of the film, even

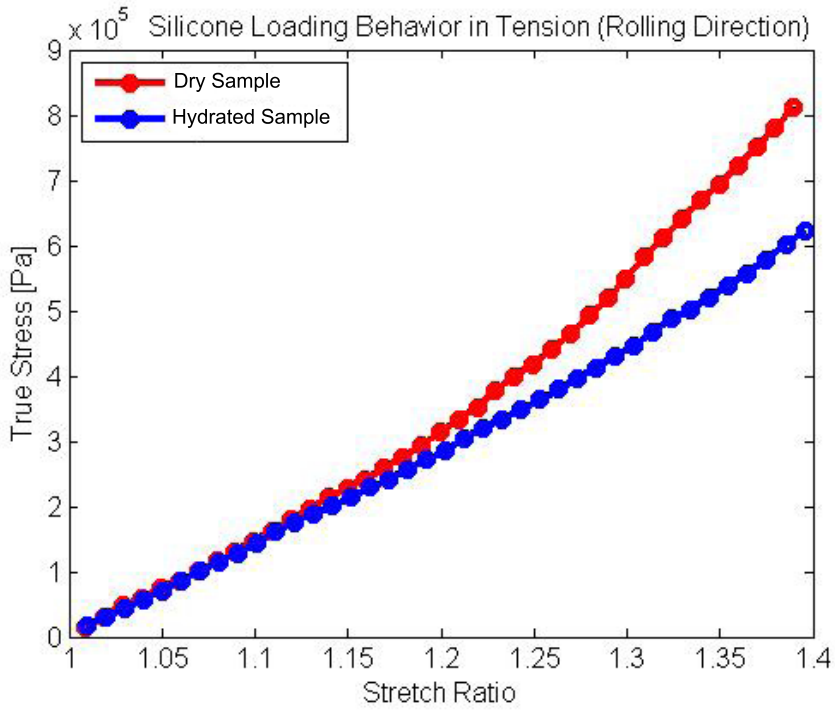

Figure 4.2: Loading behavior of silicone in tension under dry and hydrated conditions

after bonding it to the bottom plate using adhesive. However, the syringe can be adjusted to change the pressure in the chamber to a level where the film is approximately unstressed, though not flat. This can be verified by visually observing when the film goes from being symmetrically bulged to when it begins to wrinkle. The wrinkling effect of a membrane with negligible bending stiffness can be used to determine the transition from tension to compression. (This procedure is similarly done in tension tests when the material is very soft and determination of an unstressed state prior to testing is necessary.) After the zero-stress state is estimated, the center-point height of the film is measured and recorded using the displacement sensor prior to beginning the test. This measurement can be obtained by recording the distance from the sensor to the top plate and then to the center of the membrane, and, since the plate thickness is known, the center-point initial height of the film can be determined with an accuracy on the order of about 20 μm.

Again, since the properties of the polymers tested in this study are sensitive to moisture, it is important that the tests be conducted on either dry or fully hydrated specimens. Since the bottom of the film is exposed to the liquid in the chamber, the top must be hydrated as well, which requires

that the displacement sensor be able to measure through a layer of water. (Tests were conducted on films in which the top of the specimens were not hydrated, and this resulted in significant error when compared to data obtained from tension tests.) Using the capability of the confocal measuring system, the film displacement was monitored through the water layer. The water layer was kept relatively thin (less than 10 mm) to prevent the assumption of uniform stress distribution in the film from being violated and affecting the interpretation of the results.

The latex rubber was tested using both the rectangular (plane-strain) and circular geometries, with the dimensions of the former being 15 x 61 mm^2 and the latter having a diameter of 25.4 mm. The silicone rubber exhibited some anisotropy in the in-plane dimensions and was not tested using the circular configurations since the deformation was no longer axisymmetric. Therefore, for the silicone sheets the experiments were only conducted using the plane-strain configuration with the sheets aligned either with the forming direction or the direction perpendicular to the forming direction. These are referred to hereafter as the rolling and anti-rolling directions, respectively.

4.2 Characterization of Latex Rubber

4.2.1 Plane-Strain and Circular Bulge Test Results

The pressure and center-point displacement measurements were taken from three repeated experiments using both the plane-strain and biaxial configurations. A representative plot of the raw data from an experiment in which latex is tested using the circular bulge test is given in Figures 4.3 and 4.4. Figure 4.3 shows that the center-point displacement profile in time is completely linear and that the displacement rate is directly correlated with the actuation rate of the motor. Also, note that the pressure signals are completely in phase with the displacement signals, indicating that their is no viscous or time-dependent behavior exhibited by the latex. Figure 4.4 shows the same data, but instead the pressure is plotted as a function of the center-point displacement. Here, a slight hysteresis is observed in the loading and unloading curve, a phenomenon that will be explored in detail in Section 4.4.

Because of the nonlinear relationship between center-point displacement and strain using the pressure-bulge test, the strain rates will not be constant during loading even though the center-point displacement rate is constant. This is an inherent limitation with the pressure-bulge technique. Nevertheless, center-point displacement rates were varied over three different values of 0.3 mm/s, 0.6 mm/s, and 1.2 mm/s and, as mentioned previously, no strain-rate dependence was observed.

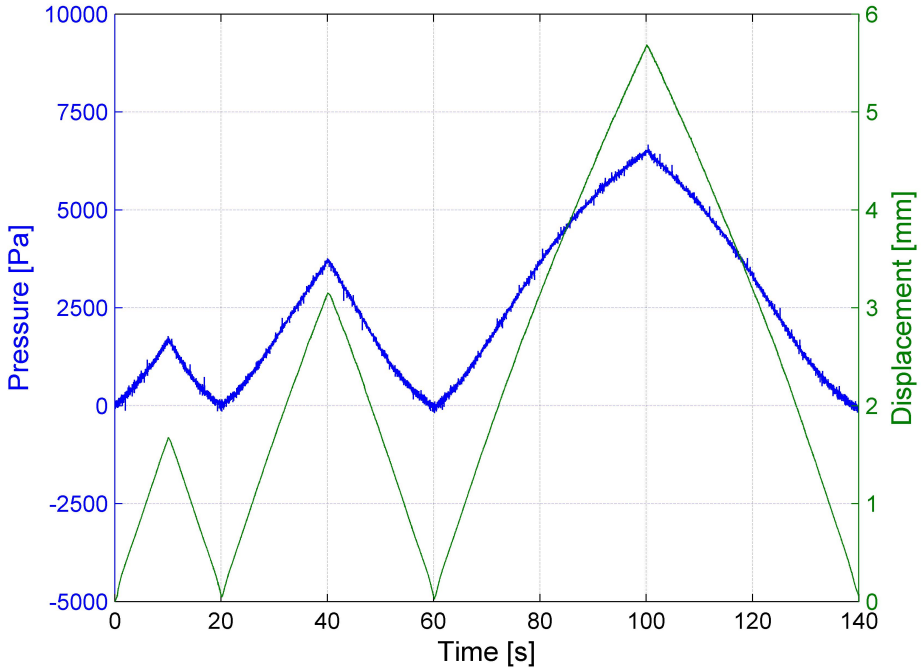

Figure 4.3: Raw pressure and center-point displacement time profiles for latex from the circular bulge test

The pressure and displacement data were converted to stress and stretch data using Eqs. (2.11)-(2.18) presented in Chapter 2 for a pressurized membrane with an initial height. Figures 4.5 and 4.6 show the true stress vs. stretch behavior of hydrated latex under plane-strain and biaxial loading configurations, respectively. These experiments were conducted over three cycles, with each cycle loading to higher stretch values. Additionally, Figure 4.7 shows a comparison between the plane-strain results and the biaxial results. As expected the biaxial configuration provides a stiffer response due to the fact that for the same values of E and ν, the biaxial modulus will always be greater than the plane-strain modulus, i.e. $B \geq M$ for the same material. During post-processing

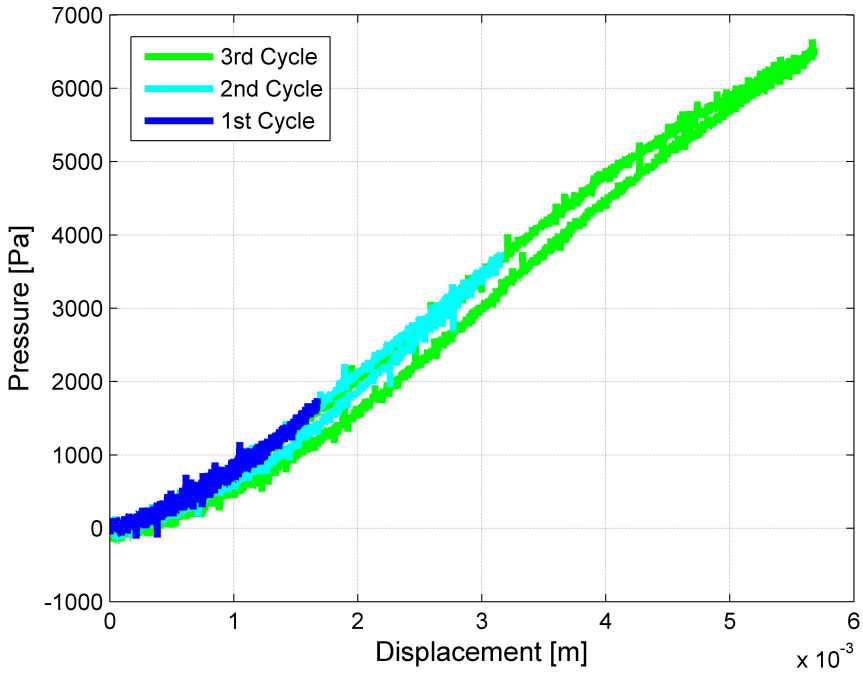

Figure 4.4: Raw pressure vs. center-point displacement data for latex over three cycles from the circular bulge test

using MATLAB, this data was filtered using a low-pass filtering algorithm and then down-sampled for better presentation. However, the determination of the constitutive behavior of the materials was accomplished using only the filtered data profiles, and not the down-sampled profiles seen in Figures 4.5 - 4.7.

Figure 4.8 contains plots of pressure vs. center-point displacement for loading data over repeated tests using both the plane-strain and biaxial bulge configurations. The data here is not expected to be very repeatable due to the fact that each test started at different initial states and therefore required the measurement of the initial center-height for each sample. The typical values these initial center-point displacements fell in the range of 2-3 mm. Due to the variations in the initial state of the membranes, these plots are normalized by the inclusion of the initial center-height in the equations presented in Section 2.3 of Chapter 2 for determination of stress and stretch of an initially non-flat membrane. Figure 4.9 shows that the measurements are relatively repeatable when the stress vs. stretch loading curves are compared over these tests. It is worth noting that both

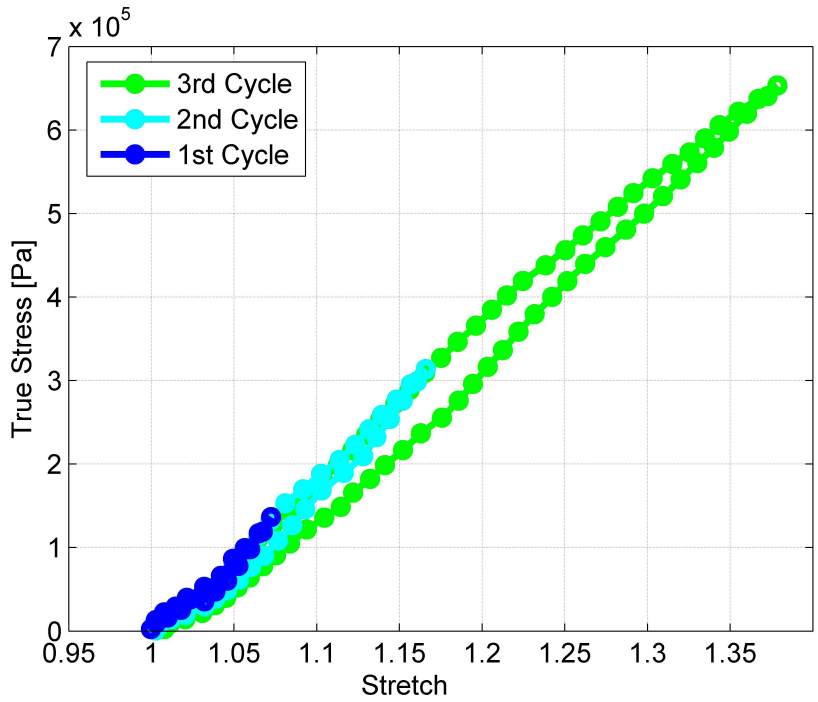

Figure 4.5: True stress vs. stretch data for latex over three cycles from the plane-strain bulge test

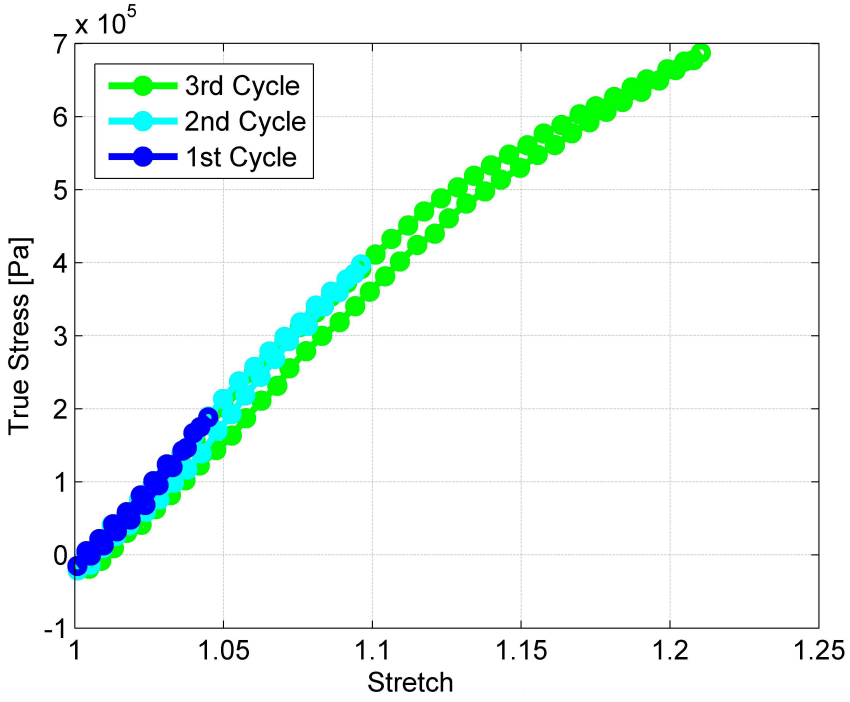

Figure 4.6: True stress vs. stretch data for latex over three cycles from the circular bulge test

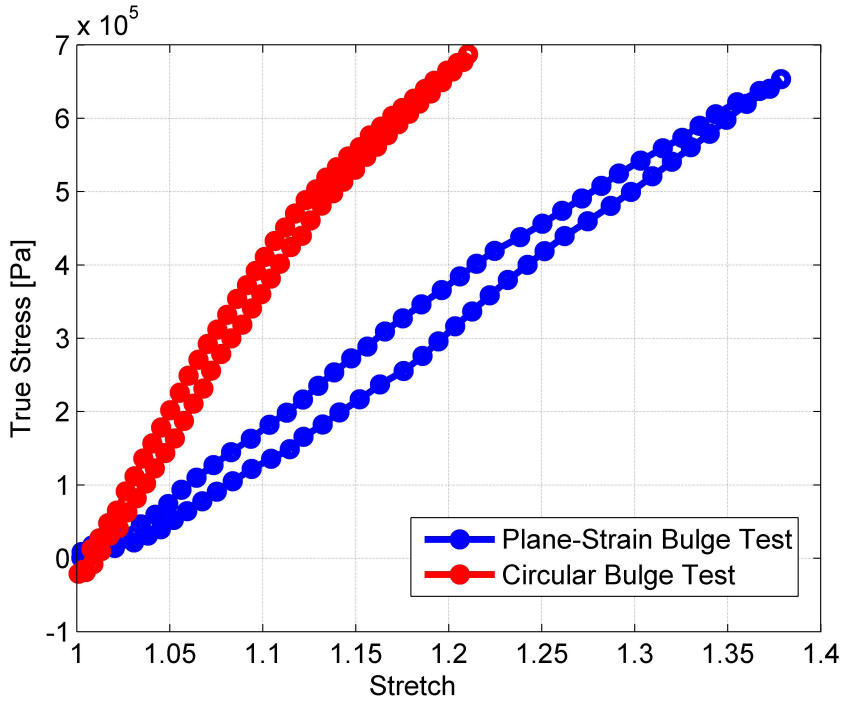

Figure 4.7: Comparison of plane-strain and biaxial true stress vs. stretch behavior for latex

the biaxial test #1 and plane-strain test #1 show softening effects with respect to the four other measurements. This is most likely due to latex degradation over time, since new latex samples were ordered in between the aforementioned tests and tests #2 and #3 for both configurations. This observed softening, which is more pronounced at higher deformations, had a slight effect on the modulus values, and as a result, modulus determination for the latex samples was analyzed using only data from tests #2 and #3.

4.2.2 Neo-Hookean Large Deformation Models under Various Loading Conditions

Latex is a classic incompressible rubber whose properties are well known. As a result, latex data obtained from the plane-strain, biaxial, and uniaxial tension tests were fit to neo-Hookean large deformation models given by the equation for true (Cauchy) stress, Σ_{ij}, as

$$\Sigma_{ij} = -\alpha\delta_{ij} + \mu F_{ij}F_{ji}, \tag{4.1}$$

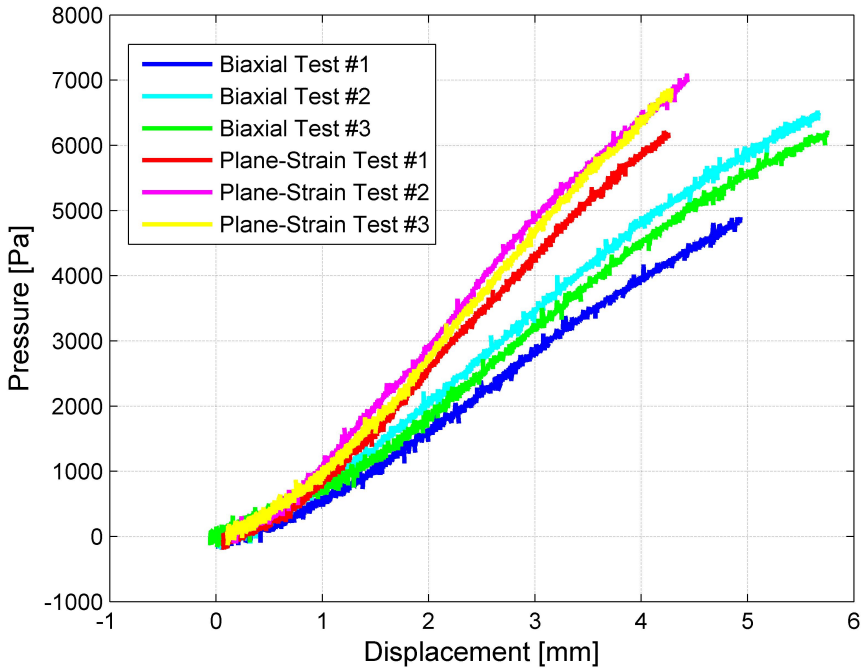

Figure 4.8: Pressure vs. center-point displacement loading data for latex from multiple plane-strain and biaxial tests

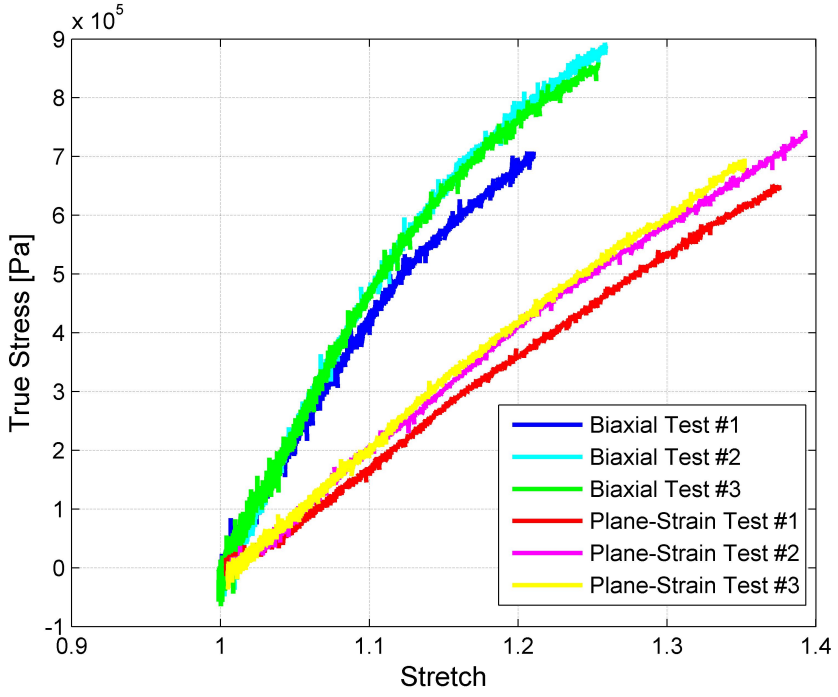

Figure 4.9: True stress vs. stretch loading data for latex from multiple plane-strain and biaxial tests

where α is a constant determined by the loading conditions, δ_{ij} is the Kronecker delta, μ is a fitting parameter related to the shear modulus, and F_{ij} is the deformation gradient. For the case of isochoric (volume preserving) deformations, the determinant of the deformation gradient must equal unity, i.e., $det(F_{ij}) = 1$. This provides a mathematical condition that allows for the deformation gradient in any loading configuration to be written solely in terms of the applied stretch in a given direction.

For the case of plane-strain, we assume that the stretch, λ, is applied in the x_1-direction and that no deformation happens in the x_2-direction, so that the deformation gradient, F_{ij}, is given as,

$$F_{ij} = \begin{pmatrix} \lambda & 0 & 0 \\ 0 & 1 & 0 \\ 0 & 0 & \frac{1}{\lambda} \end{pmatrix}, \tag{4.2}$$

which provides a relation between Σ and λ in the x_1-direction under plane-strain conditions,

$$\Sigma = \mu(\lambda^2 - \frac{1}{\lambda^2}). \tag{4.3}$$

Similarly, for the case of biaxial loading in the $x_1 - x_2$ plane, the deformation gradient and resulting Σ vs. λ relation can be written as,

$$F_{ij} = \begin{pmatrix} \lambda & 0 & 0 \\ 0 & \lambda & 0 \\ 0 & 0 & \frac{1}{\lambda^2} \end{pmatrix}, \tag{4.4}$$

$$\Sigma = \mu(\lambda^2 - \frac{1}{\lambda^4}). \tag{4.5}$$

Finally, for uniaxial tension in the x_1-direction,

$$F_{ij} = \begin{pmatrix} \lambda & 0 & 0 \\ 0 & \frac{1}{\sqrt{\lambda}} & 0 \\ 0 & 0 & \frac{1}{\sqrt{\lambda}} \end{pmatrix}, \tag{4.6}$$

$$\Sigma = \mu(\lambda^2 - \frac{1}{\lambda}). \tag{4.7}$$

4.2.3 Determination of Young's Modulus and Poisson's Ratio

The data obtained for latex from the bulge tests are compared with data obtained from uniaxial tension tests using a mechanical testing machine (Model # 5542, Instron, Norwood, MA, USA). The data from both of the bulge test configurations and from tension tests are fit using the neo-Hookean models presented above and are shown in Figures 4.10 and 4.11. The fits to these data provide values for the material parameter, μ, and the figures show that the data fits reasonably well with the neo-Hookean model with $R^2 \geq 0.99$ for each case. For a neo-Hookean material, $E = 3\mu$ is used to calculate the Young's modulus from fits to uniaxial tension data by assuming that $\nu = 0.5$ as a result of incompressibility. We need not make such an assumption here regarding Poisson's ratio using the bulge test results. We know that the ratio of the μ values from the biaxial and plane-strain fitting results are a dimensionless function of ν. In fact, it can be shown that if μ_B corresponds to the value obtained from a fit to the biaxial data and similarly μ_M for the plane-strain case, then the relation, $\frac{\mu_B}{\mu_M} = 1 + \nu$, must hold (Eq. 2.29). Using these values from the data fits and Eqs. (2.28) and (2.29), E and ν were determined from the bulge test and compared to the data fits obtained from the tension experiments. These results are presented comprehensively in Table 4.4.

4.3 Characterization of Silicone Rubber

As previously mentioned, in-plane anisotropy due to the forming process prevented the characterization of the silicone using the circular bulge configuration. The experiments were instead conducted by aligning the silicone sheets in the rolling and anti-rolling directions using the plane-strain bulge

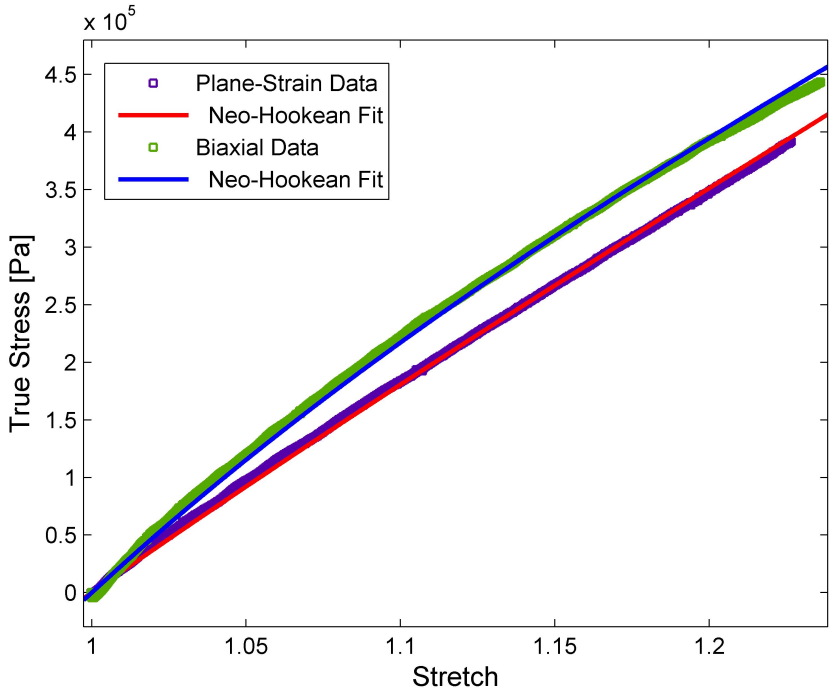

Figure 4.10: Fits of the bulge test results for latex to the neo-Hookean model for the case of plane-strain and biaxial loading, Eqs. (4.3), and (4.5), respectively

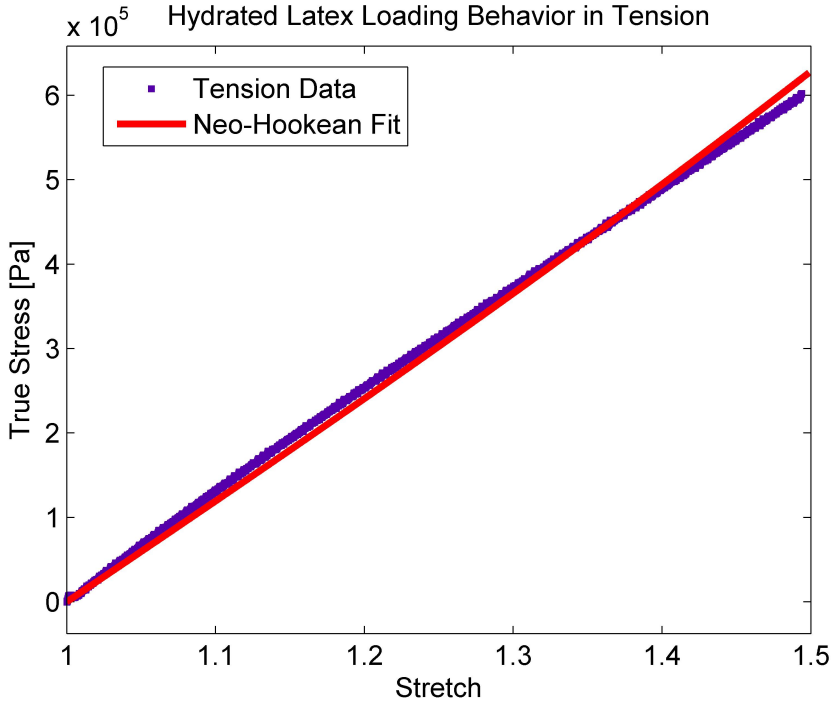

Figure 4.11: Fit of the uniaxial tension test results for latex to the neo-Hookean model Eq. (4.7)

test in tandem with uniaxial tension experiments. A representative plot of the raw data from a measurement in which silicone is tested using the plane-strain bulge test in the rolling direction is given in Figure 4.12. Again, the center-point displacement rates were varied over three different values of 0.125 mm/s, 0.25 mm/s, and 0.5 mm/s, and as with latex, no strain-rate dependence was observed for the silicone.

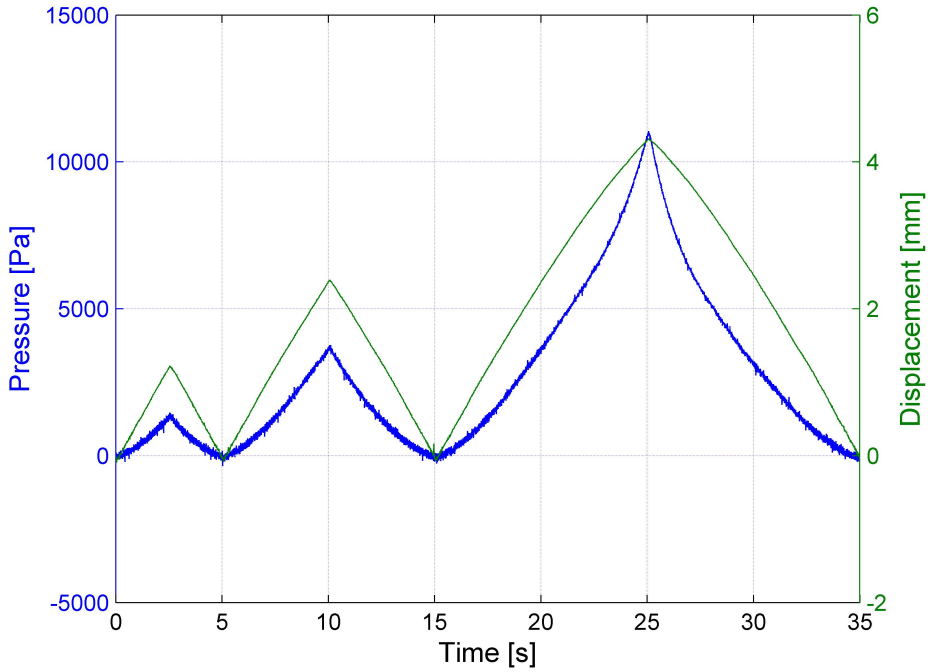

Figure 4.12: Raw pressure and center-point displacement time profiles for silicone in the rolling direction from the plane-strain bulge test

Figures 4.13 and 4.14 show the loading and unloading behavior of silicone over three cycles with each cycle going to higher strains for sheets aligned in both the rolling and anti-rolling directions. Figure 4.15 highlights the in-plane anisotropy and shows the extracted modulus values in the rolling direction were found to be higher than in the anti-rolling direction. Once again, we observe hysteresis in the loading and unloading curves as with latex.

The silicone true stress vs. stretch data did not fit as well to the neo-Hookean analytical model as did latex, as is shown in Figure 4.16. So instead of using a large deformation model to calculate the elastic constants, fits to the linear portion of the plane-strain bulge test and tension data were used

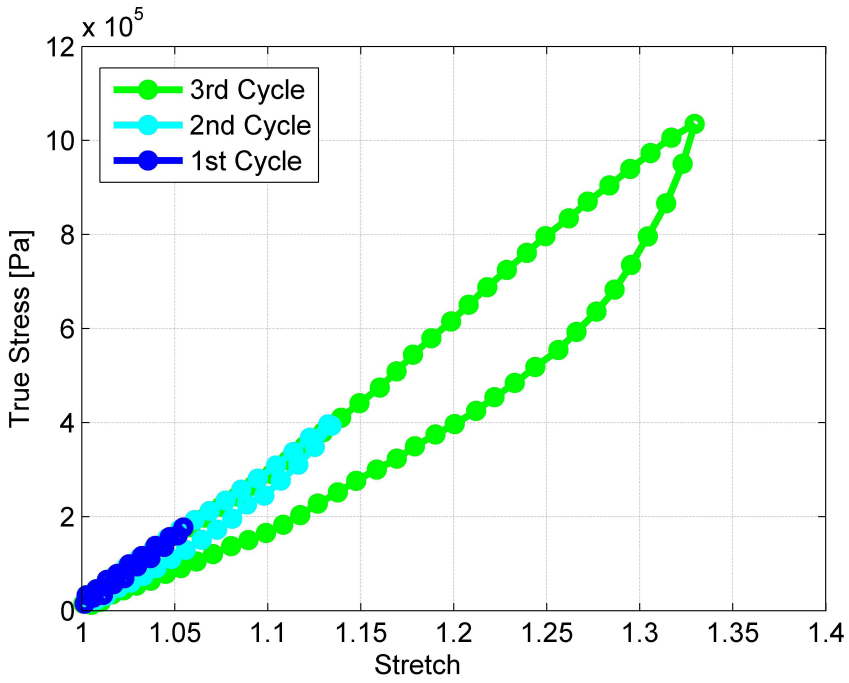

Figure 4.13: True stress vs. stretch data for silicone over three cycles in the rolling direction from the plane-strain bulge test

to determine the respective moduli. The following equations were used to evaluate the anisotropy:

$$M_r = \frac{E_r}{1-\nu_r^2}, \tag{4.8}$$

$$M_\perp = \frac{E_\perp}{1-\nu_\perp^2}, \tag{4.9}$$

and

$$\frac{E_r}{E_\perp} = \frac{\nu_r}{\nu_\perp}, \tag{4.10}$$

where M_r and $M_\perp$ are the plane-strain moduli in the rolling and anti-rolling directions (resp.) determined from the bulge test data, E_r and $E_\perp$ are the Young's moduli in the rolling and anti-rolling directions (respectively), and ν_r and $\nu_\perp$ are the Poisson's ratio in the rolling and anti-rolling directions (respectively). M_r is determined from a linear fit to the initial portion of the plane-strain

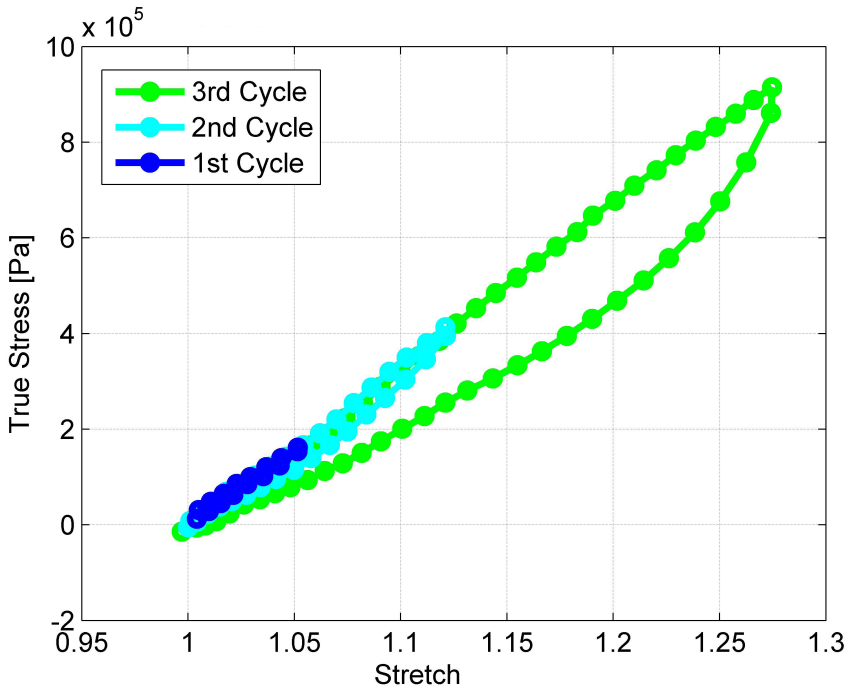

Figure 4.14: True stress vs. stretch data for silicone over three cycles in the anti-rolling direction from the plane-strain bulge test

data, and E_r is subsequently calculated using 4.8, in which ν_r is assumed to be 0.5. Also, E_r is separately determined from a fit to the initial portion of the loading curve obtained from a uniaxial tension test, and the results from the bulge and tension tests agree very well. The values for E_r are given as 1.60±0.12 MPa from the bulge test compared with 1.61 MPa extracted from the tension test. When this same method was applied to the anti-rolling direction, the results did not agree well. Therefore, Eq. 4.10 was used to determine $\nu_\perp$ by assuming that the silicone sheets used in the study are transversely isotropic. Using only values of E_r and $E_\perp$ obtained from the tension tests, an expected value of 0.48 was obtained for $\nu_\perp$. We can then use 4.9 to determine the value of $E_\perp$ from the bulge test. This value did not agree very well with the value obtained in tension, and perhaps the reason is because the material is not transversely isotropic. Alternatively, this deviation could also be due to the high level of experimental error with respect to the small degree of anisotropy in the material. The exact cause of the measurement difference is unknown since there is no information present regarding the out-of-plane behavior. A summary of the elastic constants for silicone can also

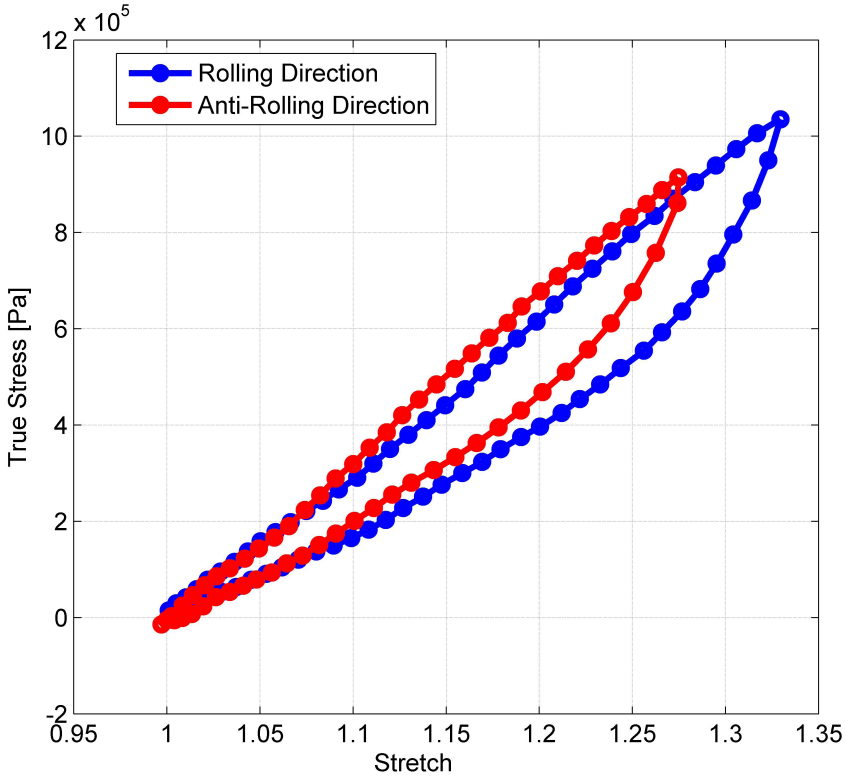

Figure 4.15: Comparison of true stress vs. stretch data for silicone in the rolling and anti-rolling directions from the plane-strain bulge test

be found in Table 4.4.

4.4 Discussion

Hysteresis is observed in the loading and unloading curves of both the latex and silicone rubber sheets. This is believed to be due to the Mullins effect of filled rubbers, however the there is insufficient information from the silicone manufacturer to conclude this definately. Mullins observed in 1948 that vulcanized rubbers with fillers under cyclic loading to the same elongation experience a softening effect in the cycles following the initial loading curve [5]. However, if the load is increased beyond the initial elongation, then Mullins observed that the curve would continue along the path of the initial curve [5]. As a result, three-cycle tests to increasing strains were conducted to determine if the observed hysteresis was the same effect observed by Mullins or an artifact of the test. From

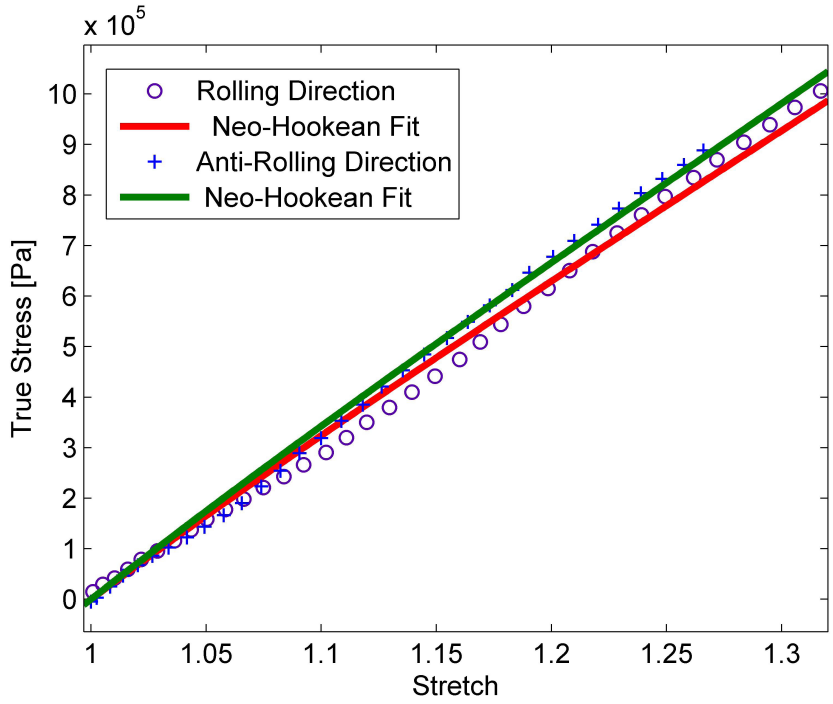

Figure 4.16: Fits of the plane-strain bulge test results to the neo-Hookean model (Eq. 4.3) for silicone

the figures it is seen that this effect does not change the elastic recovery, even though some energy is lost, and upon reloading the curves continue along the path of the previous cycle. This is consistent with Mullins effect and this characteristic is also seen in the data from the tension tests. As a final note, repeated elongation of a vulcanized rubber sample to the same strain level will eventually dampen the hysteresis, and the stress-strain behavior tends toward an equilibrium state, otherwise known as mechanical conditioning or material shakedown [5]. Mullins effect does not appear to have any impact on the values for modulus and Poisson's ratio presented here, since these values were extracted from the initial curves for each test using a new sample.

The uncertainty values presented for the elastic constants in Table 4.4 were determined from the experimental errors since these errors dominated the fitting errors. The tests were repeated three times for each sample type and bulge test configuration. The modulus values obtained from fits to the latex and silicone data were averaged and the standard deviation from the averaged value was used to quantify the experimental error. Once the experimental error for the plane-strain and

biaxial moduli were determined, then the uncertainties in Young's modulus and Poisson's ratio were deduced. It should be noted that small errors in the determination of modulus values causes a pronounced uncertainty in the Poisson's ratio calculation due to the sensitivity of the parameter. The major sources of experimental error are believed to be attributed to measurement of initial height and determination of the center-point of the membranes. The major sources of the fitting errors are attributed to noise in the pressure measurement (even after filtering) and in the case of the silicone data, linear fits to the initial portion of the curves.

Because it was known *a priori* that the latex and silicone were incompressible rubbers, it was then expected that the pressure-bulge experiments, if working properly, would provide values of Poisson's ratio that were close to 0.5. Also, data comparison with tension experiments allowed for a direct comparison of the accuracy of the bulge test experiments with a conventional testing technique. The pressure-bulge technique using an initial deflection model, Eqs. (2.11)-(2.18), for hyperelastic materials has shown major viability in being able to characterize this class of soft materials with at least as good an accuracy as testing in uniaxial tension, and with the added benefit of being able to determine the Poisson's ratio uniquely.

Material	$M = \frac{E}{1-\nu^2}$ (MPa)	$B = \frac{E}{1-\nu}$ (MPa)	E (MPa) (Bulge test)	ν (uncertainty)	E (MPa) (Tension test)
Latex	1.64±0.07	2.48±0.01	1.21±0.11	0.51 (0.07)	1.19
Silicone (rolling)	2.14±0.16	n/a	1.60±0.12	0.5 (assumed)	1.61
Silicone (anti-rolling)	1.82±0.06	n/a	1.40±0.05	0.48 (by Eq. 4.9)	1.56

Table 4.1: Summary of elastic constants determined from bulge tests and uniaxial tension tests for hydrated latex and silicone rubber samples

Chapter 5

Characterization of Hydrogels

Hydrogels are a general class of crosslinked natural or synthetic polymers that are characterized by their super-absorbability and high water content [7]. The type of hydrogel studied here is an agarose gel, which is a natural macromolecule of polysaccharide extracted from marine red algae [6, 26]. In general, polysaccharides are complex carbohydrates that are known to be amorphous and insoluble in water, and in the case of agarose and other gels, this leads to the complex microstructure of a porous solid filled with fluid [6, 8, 26]. Additionally, agarose gels can be made at different weight percentages by varying the amount of purified agarose in solution prior to gelation, which alters the microstructure and subsequent bulk mechanical behavior significantly [6, 26]. In this sense, agarose gels are categorized by their weight percentages, meaning that a 1% agarose gel is defined by 1 g of agarose powder (agar) per 100 mL of buffer solution. The type of buffer solution used to make agarose is generally a TBE buffer, which is a tris base, boric acid, and EDTA (ethylene diamine tetraacetic acid) mixture produced at various concentrations in water.

Agarose is often used in gel electrophoresis for DNA and protein separation and as scaffolds for tissue engineering purposes [6, 8, 26]. Because agarose is a such a standard biological material used in many applications, it mechanical properties are of great interest. For example, pore size distributions greatly effect the ability of agarose to separate DNA and proteins in the process of electrophoresis. Another example comes in the ability of agarose to support the cartilage phenotype *in vitro* and act as a scaffold, so that the effects of varying mechanical conditions on cartilage formation and repair can be more easily studied in the laboratory [6, 8]. Considering the applications, agarose gels have

become a model material for investigations into the mechanical and rheological behavior of biological materials.

5.1 Materials and Methods

In this study, all of the measurements were conducted on 5% agarose gels. The agarose powder and 10x TBE buffer used were obtained from J.T. Baker (Phillipsburg, NJ, USA) and the TBE buffer was then diluted to 0.5x by the addition of purified water. The 5% agarose gels were made by mixing 0.75 g of agar with 15 mL of buffer in an Erlenmeyer flask. This solution (sol) was then sealed and baked in a convection oven at 95 °C for two hours. Baking temperatures of 90-95 °C are standard since the melting point of agar is 85 °C and the boiling point of water 100 °C, allowing for a reduction in water evaporation [6, 8, 26]. The agarose sol is known to gel at temperatures around 32-40 °C, but for faster gelation, cooling to lower temperatures is often enforced [6, 8, 26].

For the bulge test samples, two 6 x 6 in^2 borosilicate glass plates (0.25 in thick) were also heated to 95 °C. After two hours, the agarose solution was poured onto the top of one of the glass plates and then sandwiched by the other plate in the oven. A 6 x 6 in^2 inner dimension wood sleeve was placed around the two plates to prevent sliding so that the weight of the top glass plate would cause the solution to spread. This worked well due to the high viscosity of 5% agarose sols, which balanced the weight of the plate. For lower weight percentages, injection molding or casting works well in forming thin sheets of gels. The thickness of the subsequent gels is highly dependent upon the volume of solution, and as a result, the volume used was determined from experimentation to be ideal for full spreading over the plate such that the gel thickness would be around 0.5 mm. The agarose sol with the plates and sleeve were removed from the oven when the sol spread to the edge of the plates and were placed in a standard refrigerator to speed up the gelation process. After gelation, the samples were either unswelled and tested immediately in the bulge test apparatus or allowed to swell to saturation in a hydrated bath and then tested. Swelling experiments by other colleagues in the laboratory found that the absorbtion of water by agarose gel is saturated for most concentrations (1 - 10%) after 30 min in hydration. Swelling times can vary based upon the weight percentage,

however we estimate that 30 min is an upper limit. The gels that were tested immediately following gelation are referred to hereafter as unswollen specimens, whereas those that were allowed to hydrate for 30 minutes are called swollen specimens. Only the circular bulge configuration was used in this particular study with an orifice diameter of 38.1 mm. Both the swollen and unswollen samples were cut into squares that were greater than 60 x 60 mm^2, so that the sample fully covered the orifice and the circular 0-ring on the bottom plate (see Figure 3.4). All agarose samples were hydrated during testing for measurements taken from the bulge test.

For the uniaxial tension experiments, the samples were prepared in a manner similar to that for the bulge test samples. However, instead of using glass plates, a teflon mold with a dogbone impression was used. The agarose sol was poured into the dogbone impression and a razor blade was used to remove excess solution by passing the blade over the top surface of the mold. The agarose sol was then gelled at room temperature. The gauge length of the dogbone specimens used was 13 mm, the width of the gauge sections was 3 mm, and the specimens were 0.1 mm thick. Because the agarose samples were gelled under a confined area, there is a possibility that these samples were residually stressed prior to loading, but this effect was not investigated. It is assumed here that the residual stress in the samples is negligible. Again the dogbone specimens were either allowed to swell for at least 30 minutes or tested unswollen using the same uniaxial testing machine (Model # 5542, Instron, Norwood, MA, USA) as used with the latex and silicone sheets. All agarose samples were hydrated during testing for the uniaxial tension measurements. To account for the water inertia experienced during loading in tension, a calibration measurement was conducted without a sample to accurately adjust the data obtained from the tests on the agarose samples. Lastly, sandpaper was taped to both sides of each grip in the testing apparatus, and the friction between the sample and sandpaper was sufficient to reduce the effects of slipping. This method worked really well and allowed for loose clamping of the grips so that the samples would not break during the onset of loading.

5.2 Monotonic Loading of Unswollen Samples

Prior to conducting any viscoelastic measurements, the agarose gels were monotonically loaded to determine if the data from these tests agreed with modulus values published in the literature for 5% agarose gels. Normand et al. tested unswollen 5% agarose in uniaxial tension, and obtained a value of 1.34 ± 0.12 MPa for the slope of the initial portion of their stress vs. strain curves [26]. These tests were conducted at a strain rate of approximately 0.028 s^{-1}. To compare, the bulge test data was obtained by fitting the monotonic loading curves to the linear elastic model, Eq. (1.1), provided in Chapter 1. The model used to fit the pressure vs. displacement curves is

$$P = \frac{4\sigma_0 t}{a^2}h + \frac{8Et}{3a^4(1-\nu}h^3. \tag{5.1}$$

This model assumes that there is no initial deflection in the film prior to loading, and while this was never the case with the latex and silicone, the agarose gels did usually have a nearly flat initial kinematic state ($h_0 \ll a$). This is so because the agarose gels tested in this study were approximately 5-6 times thicker (0.5 - 0.6 mm thicknesses) than the latex and silicone (0.1 mm thickness), and this required at least a two-fold increase in the orifice area (from a diameter of 25.4 mm to 38.1 mm). As a result, the agarose gels were more resistant to the effects of confinement. Additionally, because the gels tested in the study are not nearly as tough as the rubbers tested previously, tight clamping was not enforced because the gels would simply fracture at the boundary. The gels were clamped just tightly enough so that they were in contact with the O-ring around the exterior of the orifice, and this was sufficient to limit slipping and rotations at the boundary. Determining the appropriate clamping pressure was the most difficult challenge in these tests, because often the gels were clamped too tightly, and thus, they would tear at the onset of loading. As expected, resolving this challenge is even more difficult for tests on softer gels of concentrations less than 5%.

Figure 5.1 shows the pressure vs. displacement loading curves for three different center-point displacement rates. It can be clearly observed that as the loading rate increases, so does the stiffness at larger deflections where the membrane stresses began to dominate. This implies that the material

response is time-dependent, which validates what others have found from tests conducted on agarose [6, 8]. Additionally, Figure 5.2 shows that for the chosen deflection, the model presented in (5.1) fits very well to the experimental data. Indeed, the slope values obtained for the fitting parameter, E, increased with the loading rate, and are given as 0.65, 0.98, and 1.12 MPa under the assumption that Poisson's ratio is 0.5, and for average strain rates of 0.004, 0.016, and 0.032, respectively. Because of the nonlinear relationship between center-point displacement and strain in the bulge test, the strain rate does not remain constant for linear increases in displacements. Therefore, these strain rates were estimated as an averaged value over the loading increment to compare with data from uniaxial tension tests. The highest slope value from these measurements (1.12 MPa) was obtained at a strain rate in the same regime used by Normand et al. for their measurements, and this value falls within the error of the value reported from their tests.

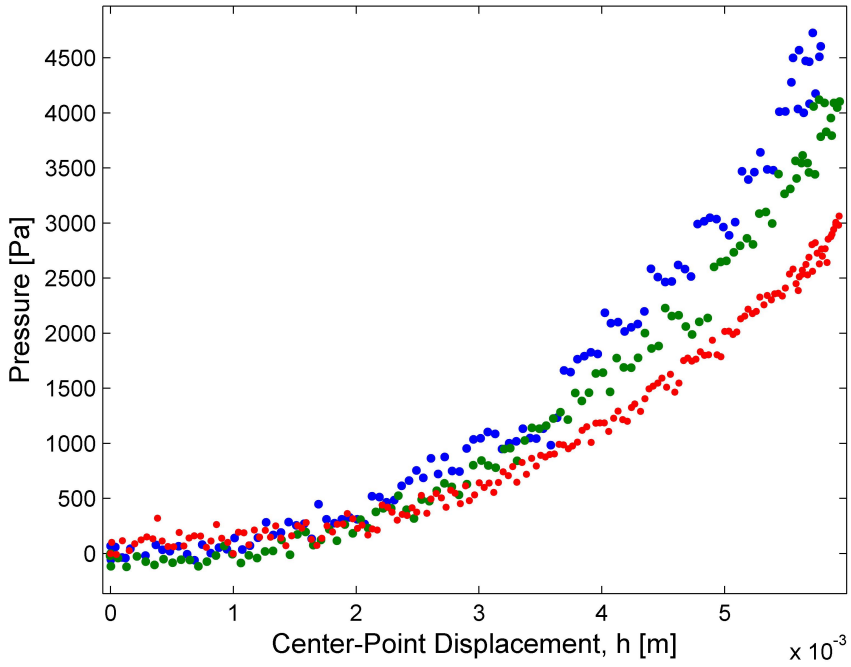

Figure 5.1: Pressure vs. displacement loading curves for unswollen 5% agarose gel over 3 different center-point displacment rates from the circular bulge test (the averaged strain rates are presented in parentheses)

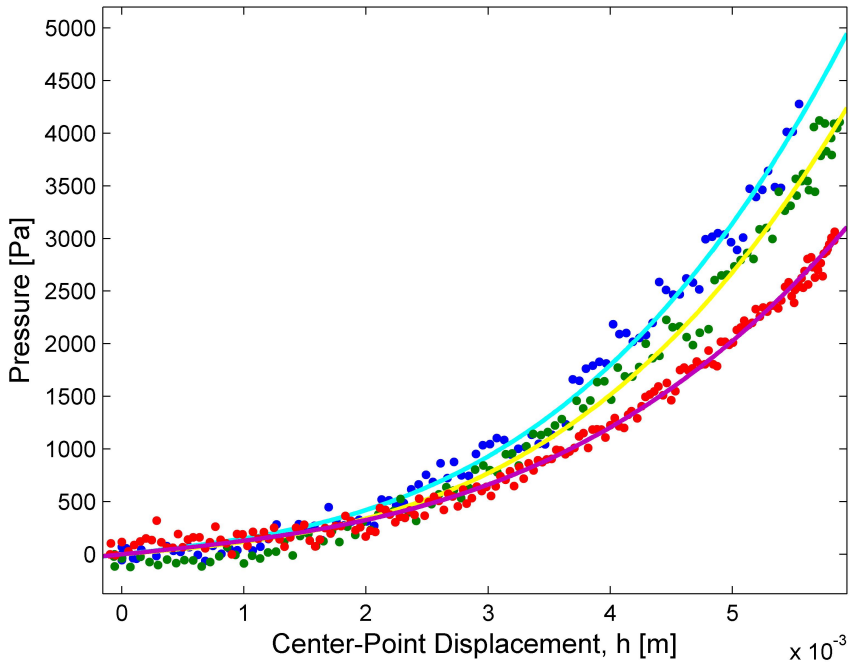

Figure 5.2: Fits of the pressure vs. displacement curves for unswollen 5% agarose gel to the pressure-displacement relation Eq. (5.1) for the circular bulge configuration

5.3 Maxwell Model for Time-Dependent Analysis

The relaxation functions for time-dependent materials obtained from stress relaxation and/or creep tests can often be modeled using a series of exponential terms. These functions are usually derived using mechanical models consisting of linear springs and dashpots. Here, the springs represent the elastic recovery of a material that is deformed, whereas the dashpot represents viscous losses in the material during loading. There are several notable mechanical models in which a variety of arrangements for springs and dashpots are considered, however, we will limit ourselves to a discussion regarding only the Maxwell model. For a more in depth treatise on the mechanical models used in linear viscoelasticity, please refer to Bland [9] or Christensen [27].

The Maxwell model is described by a spring and dashpot in series such that the total strain is given as the addition of the two strains in each element, whereas the stress in each element is the same as the total stress [9, 27]. If a step increase in strain, ϵ_0, is applied, a differential equation can be written for the stress, which has a time-decaying exponential solution [9, 27]. The stress

relaxation, $\sigma(t)$, for the Maxwell model is given as

$$\sigma(t) = [R\epsilon_0 e^{-\frac{Rt}{\eta}}]h(t), \tag{5.2}$$

where R is the linear spring constant and denotes the elastic stiffness, η is the coefficient of viscosity, and $h(t)$ is the Heaviside step function [9, 27]. The relaxation modulus in uniaxial tension, $E(t)$, is formulated by dividing the stress relaxation by the magnitude of the step increase in strain and can be written as

$$E(t) = Re^{-\frac{t}{\tau}}, \tag{5.3}$$

where τ is defined as η/R and is called the relaxation or retardation time. Multiple Maxwell models can be placed in parallel, such that the stress relaxation function can be written for an arbitrary number of Maxwell elements [9, 27]. The result is a generalized Maxwell model that is comprised of a summation of exponential terms shown here as

$$E(t) = \sum_{i=1}^{N} R_i e^{-\frac{t}{\tau_i}}. \tag{5.4}$$

For the biaxial tests using the circular bulge configuration, the result is modified to include Poisson's ratio and is given as

$$E(t) = (1-\nu)\sum_{i=1}^{N} R_i e^{-\frac{t}{\tau_i}}. \tag{5.5}$$

For the measurements in this study, $N = 2$ is chosen such that there a two characteristic stiffnesses and relaxation times for each test.

5.4 Time-Dependent Results for Swollen Agarose Samples

The aim of the tests conducted on swollen 5% agarose samples was to examine and quantify the time-dependent behavior of the gel under transverse pressure loading using the pressure-bulge technique.

The relaxation tests were performed on the agarose gels using the circular bulge configuration by ramp loading over 1.5 s to a center-point displacement of approximately 4.5 mm and holding this position over periods of 20 minutes as shown in Figure 5.3. The relaxation moduli obtained from the circular bulge tests are plotted for four different measurements and are shown in Figure 5.4 on log-log axes. The data are fit to the Maxwell model presented in the previous section, and due to the inability to enforce a step strain in the laboratory, data within times less than 12 s are excluded from the fits as shown in the figure.

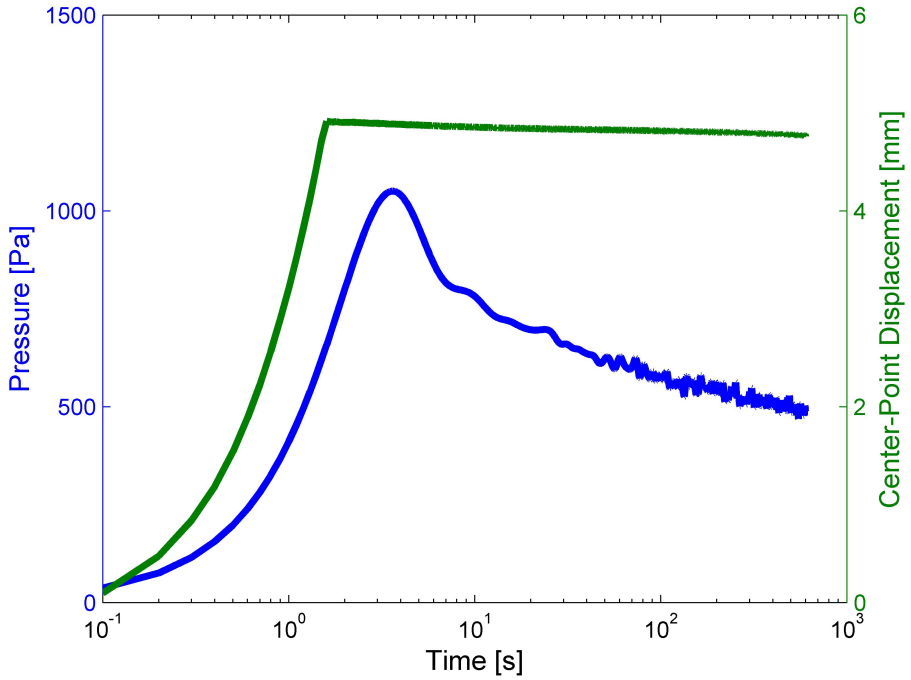

Figure 5.3: Raw data plots of pressure relaxation and center-point displacement vs. time for a swollen 5% agarose gel from the circular bulge test over 20 minutes

Relaxation tests were also performed on 5% agarose gels in uniaxial tension to compare with the results obtained from the circular bulge test. Figure 5.5 shows the raw data plots of force relaxation and displacement vs. time for a swollen 5% agarose gel obtained from a uniaxial tension test.The relaxation tests in tension were performed by ramp loading over 1 s to a dispacement of approximately 1 mm and holding this position over periods of 20 minutes. The relaxation moduli obtained from the tension tests are plotted for two different measurements and are shown in Figure

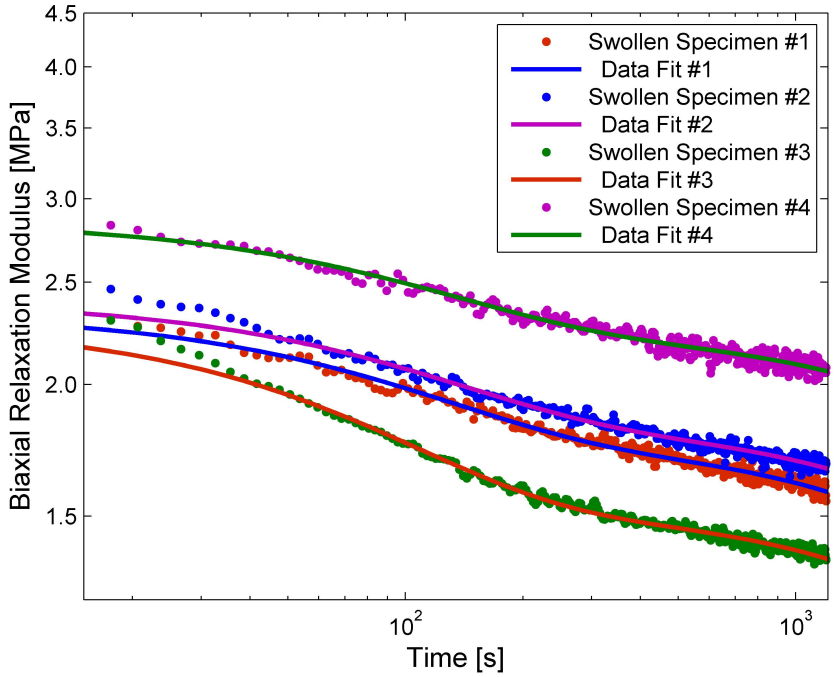

Figure 5.4: Plots of relaxation moduli vs. time fit to a Maxwell model for four measurements on swollen 5% agarose gels from the circular bulge tests over 20 minutes

5.6 on log-log axes. Again, the data are fit to the Maxwell model presented above and here data within times less than 10 s are excluded from the fits and are not shown in the figure.

As can be observed in both the relaxation tests in tension and using the bulge setup, the agarose gels displayed considerable relaxation up to testing times of 20 minutes. Therefore, the tension relaxation tests were repeated for testing times of 1 hr to determine whether are not the agarose would come to an equilibrium state for longer testing times. These tests were still conducted with a ramp time of 1 s up to a displacement of 1 mm, and the hold time was increased to 1 hr. Raw data plots of force relaxation and displacement vs. time for a typical test are shown in Figure 5.7. The relaxation moduli and data fits are shown in in Figure 5.8. In both figures, a great deal of relaxation can still be observed, even for testing times up to 1 hour.

Table 5.4 contains a summary of the fitting parameters from the Maxwell model obtained for each test conducted in this study. Additionally, the averaged values for fits to the bulge and tension test data are used in the Maxwell model to determine how well the tests agree with one another.

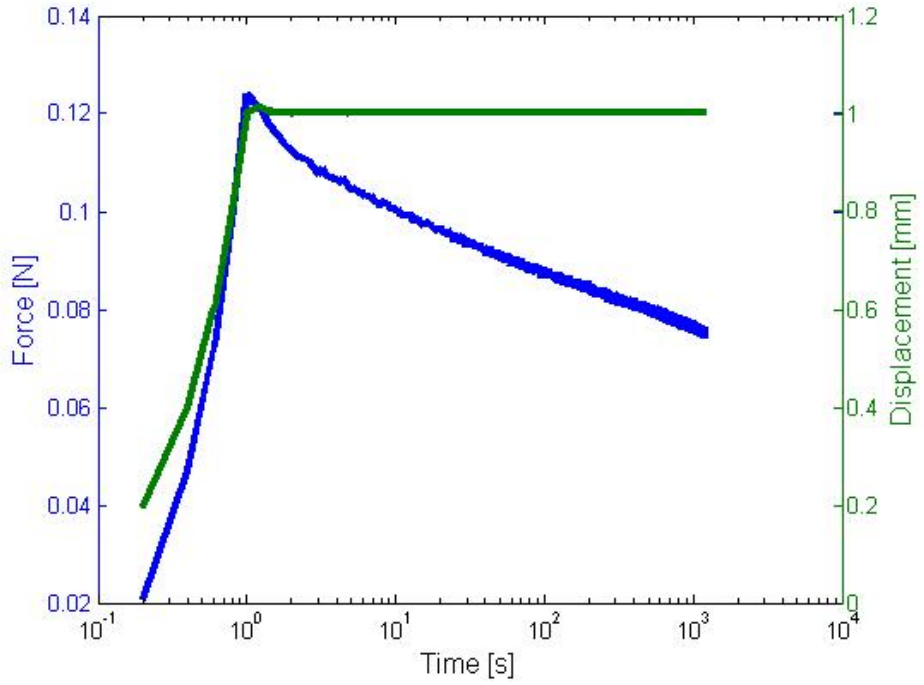

Figure 5.5: Raw data plots of force relaxation and displacement vs. time for a swollen 5% agarose gel from a uniaxial tension test over 20 minutes

Plots of these curves are shown in Figure 5.9, and the curve obtained from tension data falls within the error of the curve obtained from the bulge tests. Even so, several interesting trends can be noticed from these data. The first is that the relaxation times for the bulge tests vs. the tension tests are shorter, and this difference is outside of the experimental error for both τ_1 and τ_2. Next, the bulge test values for stiffness are higher than those obtained in tension for the same testing times. Lastly, the longer relaxation time obtained for measurements taken over 1 hr is predicted to be around 17 hours, which was unexpected. All of these observations are believed to be due to the effects of porosity and the motion of fluid through the pores of the gel network. If this hypothesis is correct, then the time-dependent behavior measured here is not due solely to the viscoelasticity of the gel, and neither the tension nor bulge tests can be used to deconvolve the pressure-dependent and the deviatoric behavior of agarose. To fully investigate these effects, tests under a pure shearing deformation should be conducted to determine the deviatoric behavior directly. Chen et al. [6] present values for viscoelastic parameters of agarose obtained from shear tests using a power-law

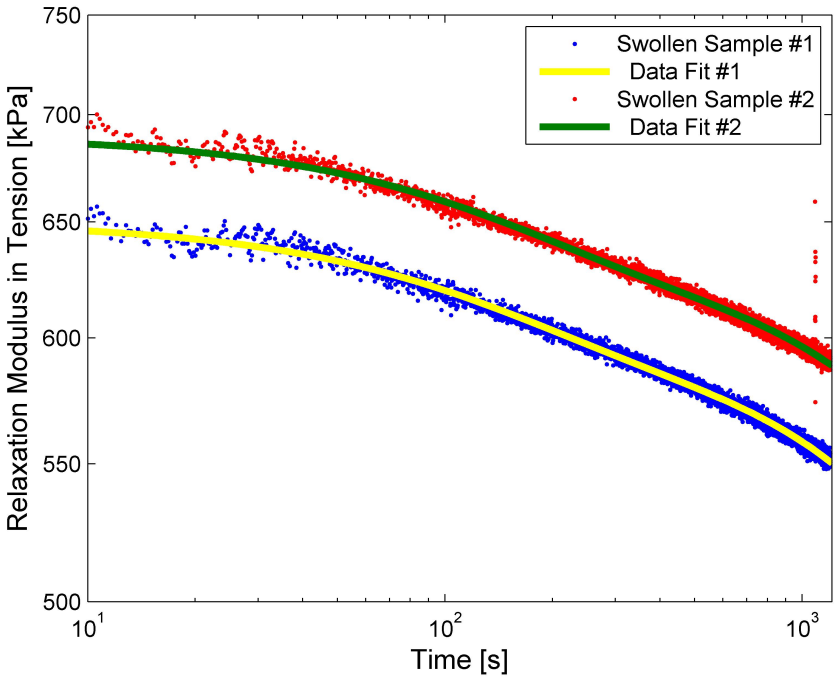

Figure 5.6: Plots of relaxation moduli vs. time fit to a Maxwell model for two measurements on swollen 5% agarose gels from uniaxial tension tests over 20 minutes

model, and those results seem to indicate a lower degree of time-dependency with respect to values obtained in these measurements and others by colleagues in the laboratory. Additionally, other researchers [8, 26] report differences in stiffness values obtained from testing using different loading configurations. Chiarelli et al. [7] studied the dynamics of a hydrogel strip in tension and found that their samples, made of polyvinyl alcohol-polyacrylic acid, fit well to a poroelastic continuum model derived for the gel-solvent system. Similarly, to truly understand the behavior of agarose gels, more sophisticated models that account for porous and fluid effects may be needed.

	R_1 (kPa)	τ_1 (s)	R_2 (kPa)	τ_2 (hr)	Testing Time
Bulge Test	312 ± 47	109 ± 14	925 ± 151	3.23 ± 0.35	20 min
Tension Test	54 ± 4	148 ± 7	616 ± 25	4.25 ± 0.40	20 min
Tension Test	33 ± 11	519 ± 36	439 ± 111	17.1 ± 0.70	1 hr

Table 5.1: Summary of the time-dependent parameters for 5% agarose using two Maxwell models in parallel Eqs. (5.4) and (5.5) determined from fits to data from relaxation tests in tension and the pressure-bulge technique

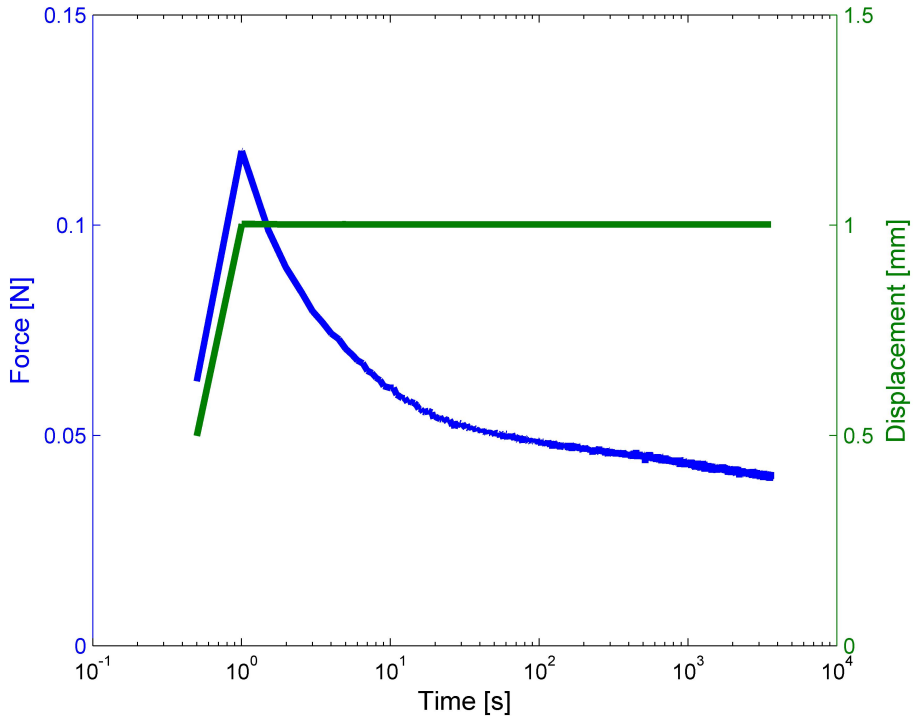

Figure 5.7: Raw data plots of force relaxation and displacement vs. time for a swollen 5% agarose gel from a uniaxial tension test over 1 hour

5.5 Wrinkling and the Effects of Relaxation

One of the early goals of this work was to use the pressure-bulge technique to conduct oscillatory loading experiments on a viscoelastic material. As a result, this required the ability to conduct cyclic loading and unloading experiments on the material. As has been observed in the earlier sections, 5% agarose displays a great deal of viscous behavior under loading, which causes significant loss in energy upon unloading. As a result, when the agarose membranes were loaded and unloaded, at some point during the unloading the membrane would wrinkle before going back to its original position as shown in Figure 5.10. This is because for the film to return to its initial position, it would have to exist in a state of compression away from the boundary where it is more compliant, and membranes can not sustain compressive stresses without wrinkling [30]. The pressure and displacement time profiles for the loading and unloading behavior of agarose are provided in Figure 5.11. The pressure vs. center-point displacement plot for the same data is also provided in Figure 5.12, and it is clearly

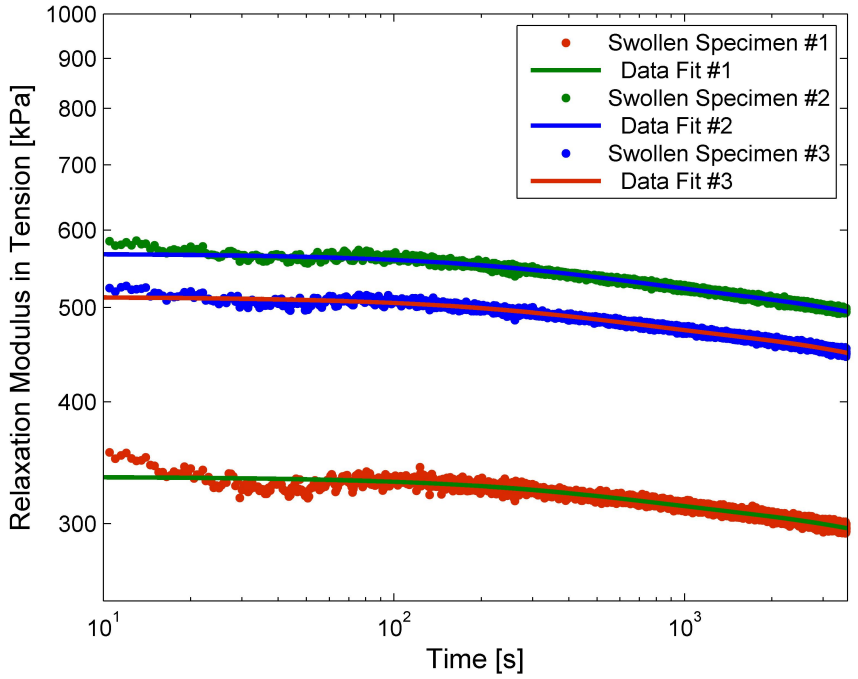

Figure 5.8: Plots of relaxation moduli vs. time fit to a Maxwell model for three measurements on swollen 5% agarose gels from uniaxial tension tests over 1 hour

observed here that the transverse pressure reaches zero well before the center-point displacement goes to zero due to film relaxation.

Cyclic experiments were conducted to determine what if any effects the wrinkling phenomena would have on viscoelastic characterization under oscillatory loading. Referring to Figure 5.13, cyclic pressure and center-point displacement time profiles for 5% agarose are shown and repeatable wrinkling events occur during each loading and unloading profile following the initial loading curves. This same data is presented in Figure 5.14 as pressure vs. displacement plots for the first three loading and unloading cycles. These plots show that the observed wrinkling phenomenon is completely reversible, which implies that no irreversible deformation, such as plasticity or film slipping, is occuring during the experiment. This wrinkling phenomenon is consistent over multiple tests, and it is unclear at this point how cyclic loading can be conducted using this configuration to determine frequency-dependent information.

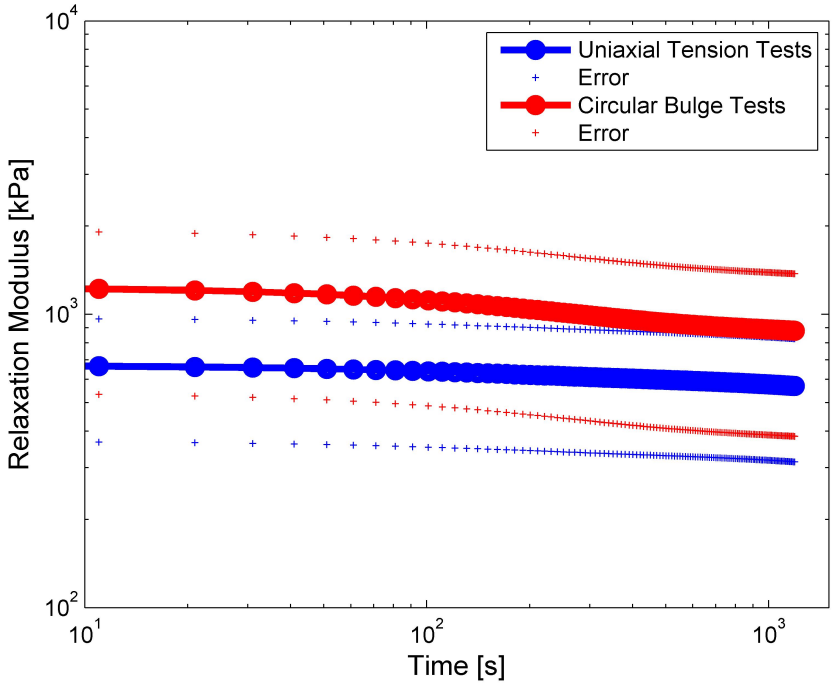

Figure 5.9: Comparison of the time-dependent response of 5% agarose obtained from fits to tension and bulge test data for a testing time of 20 minutes

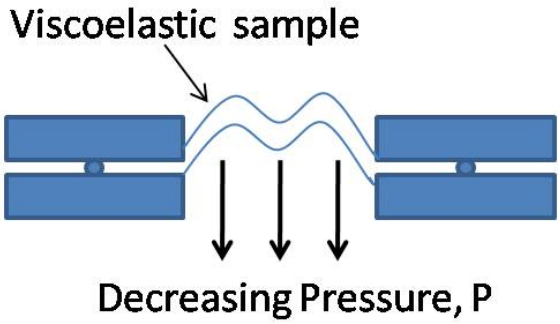

Figure 5.10: Schematic of a viscoelastic clamped membrane buckling under decreasing pressure after stress relaxation during initial loading

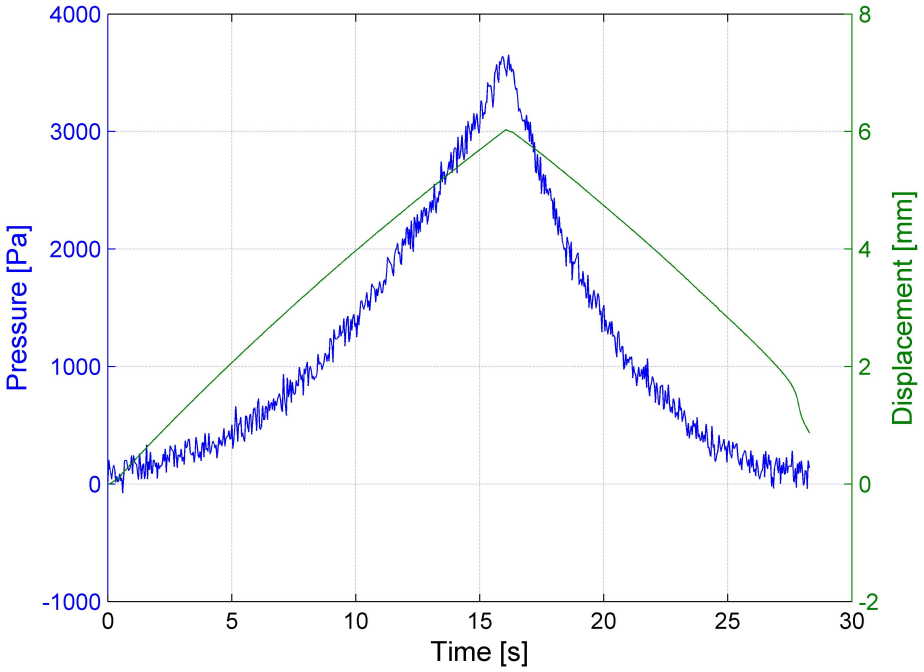

Figure 5.11: Pressure and center-point displacement time profiles for 5% agarose under loading and unloading using the circular bulge test

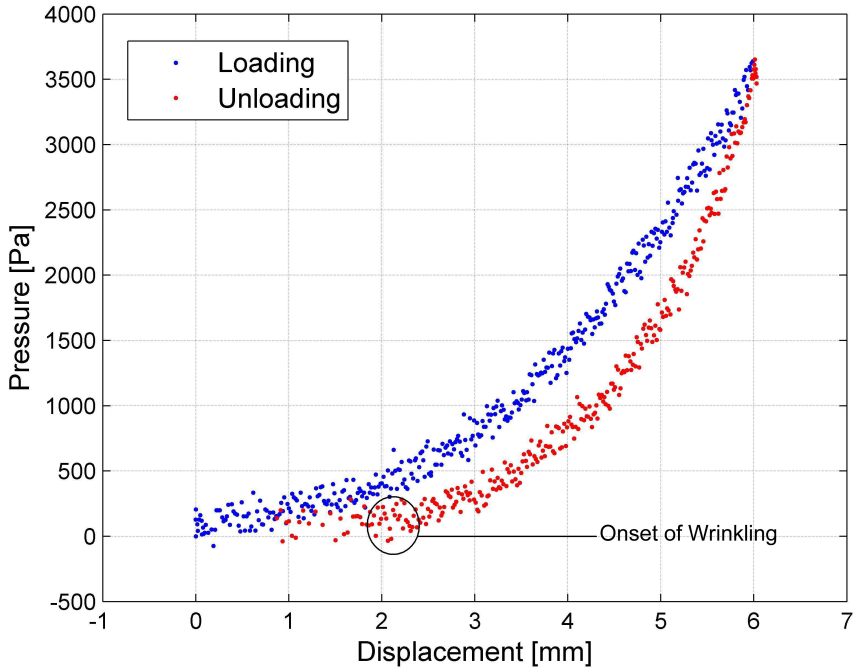

Figure 5.12: Pressure vs. center-point displacement loading and unloading behavior for 5% agarose using the circular bulge test with the onset of the film wrinkling highlighted

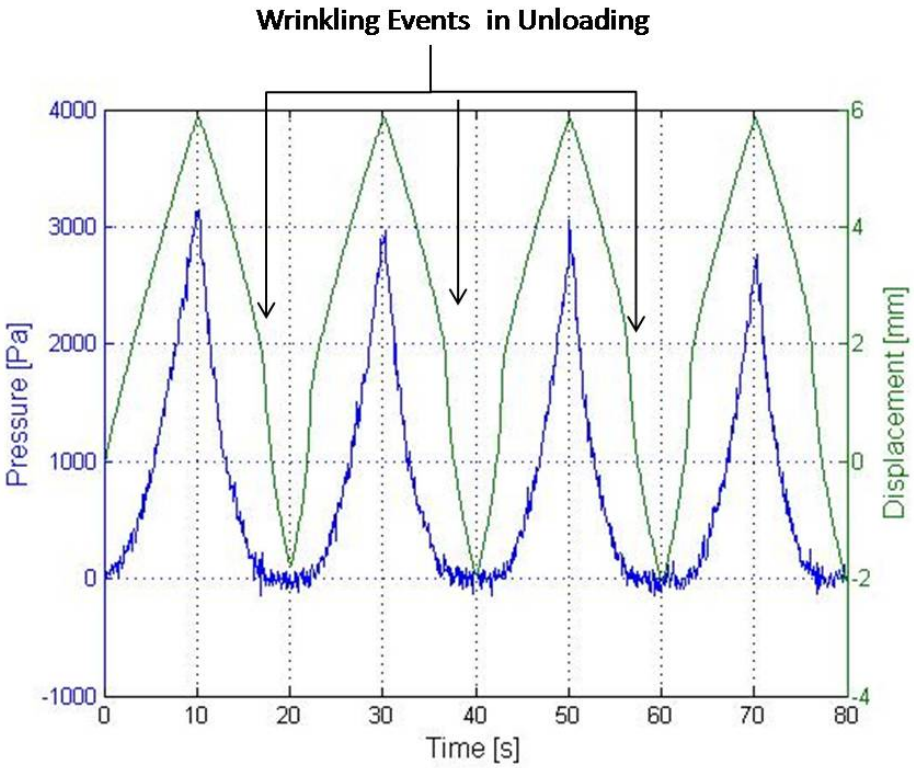

Figure 5.13: Cyclic pressure and center-point displacement time profiles for 5% agarose using the circular bulge test with repeatable wrinkling events observed

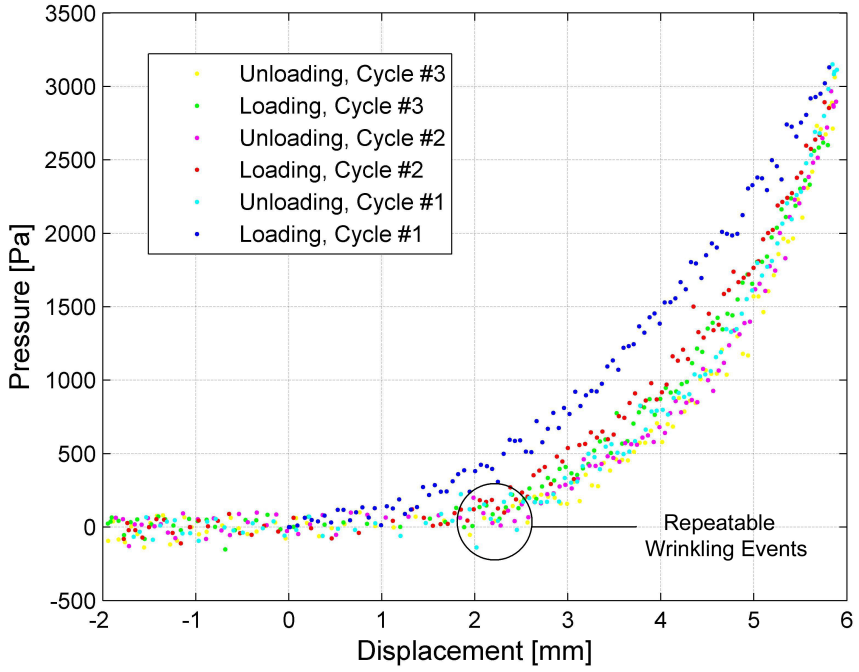

Figure 5.14: Pressure vs. center-point displacement cyclic behavior for 5% agarose using the circular bulge test with observed intercycle hysteresis and wrinkling

Chapter 6

Summary and Future Work

6.1 Summary

The previous chapters sought to provide a framework by which the commonly used pressure-bulge technique for thin-film characterization could be extended to the bulk characterization of soft polymers and hydrogels. This concept, known as membrane inflation, has been around since the late 1970s, but has not gained much prominence, due primarily to limitations in out-of-plane measuring techniques for materials that are optically translucent and/or that reflect little light. Here an experimental apparatus was constructed that utilized a novel confocal displacement measuring technique, and as a result the setup was able to track the center-point out-of-plane displacement of clamped polymer films. Additionally, due to the ability of the displacement sensor to focus through transparent surfaces, hydrated tests were enabled so that one could conduct tests of biological materials in their native environment and account for the effects of moisture.

The experimental facility was used first to characterize latex and silicone rubber in an effort to determine the viability of the setup. The large deformation constitutive behavior of these hyperelastic polymers were tested using circular and high-aspect-ratio rectangular bulge configurations, which provide biaxial stress and plane-strain conditions in the membrane, respectively. A nonlinear geometric model was derived to account for the presence of an initial film deflection due to the high compliance of the polymer membranes under confinement pressures from clamping. This initial deflection model was used to interpret the data from the measurements, and the results were compared

to data obtained using standard uniaxial tension tests to gage the accuracy. It was shown that the experimental facility and the initial deflection model were able to provide results consistent with those obtained from the experiments in tension.

After the model and experimental facility were validated, the pressure-bulge setup was used to characterize the time-dependent behavior of 5% agarose gels. Agarose also serves as a common biological model material, and as a result, its bulk and microstructural properties are of great interest. In this study, the stress relaxtion behavior of the 5% gels was investigated using the circular pressure-bulge test and compared to relaxation data obtained in uniaxial tension. The biaxial and uniaxial tension data were fit to a fractional derivative model, and the model was able to fit the data from both tests. Also, the behavior of agarose under cyclic loading and unloading was investigated with the circular bulge configuration. Here film buckling was observed after the initial loading in the both the unloading and subsequent loading curves. This wrinkling effect was completely reversible and was not attributed to any irrecoverable deformation, but instead was believed to be caused by the energy loss due to stress relaxation in the film during the initial loading. This wrinkling phenomena, as well as limitations in measuring capabilities, prevented the completion of additional experiments in the frequency domain.

6.2 Recommendations for Future Work

The pressure-bulge data presented in this work shows great promise for the use of the apparatus to conduct studies on other biological materials, such as tissues and cells cultured onto matrices under transverse loading and in a physiological environment. Specific examples of these applications include the characterization of arterial and lung tissues using the bulge technique, which can accurately mimic the *in vivo* mechanical conditions of pulsatile loading for the former and pressure relaxation for the latter. Additionally, researchers have looked for new ways of testing cell interactions with matrices that are mechanically stressed, and the membrane inflation tests have already proven to be a viable option for this type of experiment. Overall, the pressure-bulge technique is ideally suited for biological studies because other popular experiment techniques, such as uniaxial compression and

tension, as well as shear and torsional loading, require that sample geometries be accurately measured and controlled for repeatable data analysis. This requirement limits the application of these tests to the characterization of native tissues that cannot be cut or formed into simple geometries.

Lastly, the pressure-bulge technique has yet to be used to characterize many industrial non-metallic materials due to limitations in measuring out-of-plane displacement and models that do not account for testing conditions in which the material is not deposited onto a substrate using vapor deposition techniques. The work in this dissertation suggests that sheets of bulk material can be tested using the bulge apparatus, and the equations need only be modified to account for experimental conditions, such as negligible residual stress and time-dependent behavior. It is the hope of the author that this work will contribute in making the pressure-bulge technique a standard mechanical testing device capable of characterizing a much wider range of materials.

Bibliography

[1] M.G. Allen, M. Mehregany, R.T. Howe, and S.D. Senturia. Microfabricated structures for the *in situ* measurement of residual stress, young's modulus, and ultimate strain of thin films. *Applied Physics Letters*, 51(4):241–243, 1987.

[2] J.W. Beams. *Structure and Properties of Thin Films.* John Wiley and Sons, New York, 1st edition, 1959.

[3] F.A. Breton. *A large deformation analysis of plates or membranes for the determination of Young's modulus and Poisson's ratio.* Califonia Institute of Technology, Engineer's Thesis in Aeronautics, 1995.

[4] F.A. Breton and W.G. Knauss. Error limitations in the determination of mechanical properties of thin films. *Journal of Reinforced Plastics and Composites*, 16(1):17–32, 1997.

[5] R. Brown. *Physical Testing of Rubber.* Springer, New York, 4th edition, 2006.

[6] Q. Chen, B. Suki, and K-N. An. Dynamic mechanical properties of agarose gels modeled by a fractional derivative model. *Journal of Biomechanical Engineering: Transactions of the ASME*, 126(1):666–671, 2004.

[7] P. Chiarelli, P. Basser, D. Derossi, and S. Goldstein. The dynamics of a hydrogel strip. *Biorheology*, 29(4):383–398, 1992.

[8] P. de Freitas, D. Wirz, M. Stolz, B. Gopfert, N-F. Friederich, and A. Daniels. Pulsatile dynamic stiffness of cartilage-like materials and use of agarose gels to validate mechanical methods and

models. *International Journal of Biomedical Materials Research Part B: Applied Biomaterials*, 78(1):347–357, 2006.

[9] Bland D.R. *The Theory of Linear Viscoelasticity.* Pergamon Press, New York, International Series of Monographs on Pure and Applied Mathematics: Volume 10 edition, 1960.

[10] R.L. Edwards, G. Coles, and W.N. Sharpe Jr. Comparison of tensile and bulge tests for thin-film silicon nitride. *Experimental Mechanics*, 44(1):49–54, 2004.

[11] W.W. Feng. Viscoelastic behavior of elastomeric membranes. *Journal of Applied Mechanics*, 59(1):29–34, 1992.

[12] W.N. Findley, J.S. Lai, and K. Onaran. *Creep and Relaxation of Nonlinear Viscoelastic Materials: With an Introduction to Linear Viscoelasticity.* North-Holland Publishing Company, Amsterdam, 2nd edition, 1959.

[13] J.D. Hall, B.T. Apperson, B.T. Crozier, C. Xu, R.F. Richards, and D.F. Bahr. A facility for characterizing the dynamic mechanical behavior of thin membranes for microelectromechanical systems. *Review of Scientific Instruments*, 73(5):2067–2072, 2002.

[14] F.P.K. Hsu, A.M.C. Lui, J. Downs, D. Rigamonti, and J.D. Humphrey. A triplane video-based experimental system for studying axisymmetrically inflated biomembranes. *IEEE Transactions on Biomedical Engineering*, 42(5):442–450, 1995.

[15] F.P.K. Hsu, C. Schwab, D. Rigamonti, and J.D. Humphrey. Identification of response functions from axisymmetric membrane inflation tests: implications for biomechanics. *International Journal of Solids and Structures*, 31(24):3375–3386, 1994.

[16] S. Hyun, W.L. Brown, and R.P. Vinci. Transient creep in free-standing thin polycrystalline aluminum films. *Applied Physics Letters*, 83(21):4411–4413, 2003.

[17] A.J. Kalkman, A.H. Verbruggen, and G.C.A.M. Janssen. Young's modulus measurements and grain boundary sliding in free-standing thin metal films. *Applied Physics Letters*, 78(18):2673–2675, 2001.

[18] A.J. Kalkman, A.H. Verbruggen, G.C.A.M. Janssen, and F.H. Groen. A novel bulge-testing setup for rectangular free-standing thin films. *Review of Scientific Instruments*, 70(10):4026–4031, 1999.

[19] O. Kraft and C. Volkert. Mechanical testing of thin films and small structures. *Advanced Engineering Materials*, 3(3):99–110, 2001.

[20] K. Kurpinski, J. Chu, C. Hashi, and S. Li. Anisotropic mechanosensing by mesenchymal stem cells. *Proceedings of the National Academy of Sciences*, 103(44):16095–16100, 2006.

[21] M.D. Larson, C.J. Simonson, R.W. Besant, and P.W. Gibson. The elastic and moisture transfer properties of polyethylene membranes for use in liquid-to-air energy exchangers. *Journal of Membrane Science*, 302(1):136–149, 2007.

[22] D. Maier-Schneider, J. Maibach, and E. Obermeier. A new analytical solution for the load-deflection of square membranes. *Journal of Microelectromechanical Systems*, 4(4):238–241, 1994.

[23] E. Makino, T. Shibata, and K Kato. Dynamic thermo-mechnical properties of evaporated TiNi shape memore thin film. *Sensors and Actuators*, 78(1):163–167, 1999.

[24] E. Makino, T. Shibata, and K Kato. Dynamic actuation properties of TiNi shape memory diaphragm. *Sensors and Actuators*, 79(1):128–135, 2000.

[25] J.S. Mitchell, C.A. Zorman, T. Kicher, S. Roy, and M. Mehregany. Examination of bulge test for determining residual stress, young's modulus, and poisson's ratio of 3C-SiC thin films. *Journal of Aerospace Engineering*, 16(2):46–54, 2003.

[26] V. Normand, D. Lootens, E. Amici, K. Plucknett, and P. Aymard. New insight into agarose gel mechanical properties. *Biomacromolecules*, 1(4):730–738, 2000.

[27] Christensen R.M. *Theory of Linear Viscoelasticity: An Introduction.* Academic Press, New York, 2nd edition, 1982.

[28] J.C. Selby and M.A. Shannon. Apparatus for measuring the finite load-deformation behavior of a sheet of epithelial cells cultured on a mesoscopic freestanding elastomer membrane. *Review of Scientific Instruments*, 78(9):1–12, 2007.

[29] A. Shukla, A.R. Dunn, M.A. Moses, and K.J. Van Vliet. Endothelial cells as mechanical transducers: enzymatic activity and network formation under cyclic strain. *Mechanics and Chemistry of Biosystems*, 1(4):279–290, 2004.

[30] M. Small, B.J. Daniels, B.M. Clemens, and W.D. Nix. The elastic biaxial modulus of Ag-Pd multilayered thin films measured using the bulge test. *Journal of Materials Research*, 9(1):25–30, 1994.

[31] M. Small and W.D. Nix. Analysis of the accuracy of the bulge test in determining the mechanical properties of thin films. *Journal of Materials Research*, 7(6):1553–1563, 1992.

[32] V.T. Srikar and S.M. Spearing. A critical review of microscale mechanical testing methods used in the design of microelectromechanical systems. *Experimental Mechanics*, 43(3):238–246, 2003.

[33] O. Tabata, K. Kawahata, S. Sugiyama, and I Igarashi. Mechanical property measurements of thin films using load-deflection of composite rectangular membranes. *Sensors and Actuators*, 20(1):135–141, 1989.

[34] T. Tsakalakos and J.E. Hillard. Elastic modulus in composition-modulated copper-nickel foils. *Journal of Applied Physics*, 54(2):734–737, 1982.

[35] K. Van Vliet, G. Bao, and S. Suresh. The biomechanics toolbox: experimental approaches for living cells and biomolecules. *Acta Materialia*, 51(1):5881–5905, 2003.

[36] E. Ventsel and T. Krauthammer. *Thin Plates and Shells: Theory Analysis, and Applications.* Marcel Dekker, Inc., New York, 1st edition, 2001.

[37] J.J. Vlassak and W.D. Nix. A new bulge test technique for the determination of young's modulus and poisson's ratio of thin films. *Journal of Materials Research*, 7(12):3242–3249, 1992.

[38] B.A. Walmsley, Y Liu, X.Z. Hu, M.B. Bush, and J.M. Dell. Poisson's ratio of low-temperature PECVD silicon nitride thin films. *Journal of Microelectromechanical Systems*, 16(3):622–627, 2007.

[39] C. Waters, M. Glucksberg, E. Lautenschlager, C-W. Lee, R. Van Matre, R. Warp, U. Salva, K. Healey, B. Moran, D. Castner, and J. Bearinger. A system to impose prescribed homogenous strains on cultured cells. *Journal of Applied Physiology*, 91(1):1600–1610, 2001.

[40] A. Wineman, D. Wilson, and J.W. Melvin. Material identification of soft tissue using membrane inflation. *Journal of Biomechanics*, 12(1):841–850, 1979.

[41] Y. Xiang, X. Chen, and J.J. Vlassak. Plane-strain bulge test for thin films. *Journal of Materials Research*, 20(9):2360–2370, 2005.

[42] C. Zhu, G. Bao, and N. Wang. Cell mechanics: mechanical response, cell adhesion, and molecular deformation. *Annual Review of Biomedical Engineering*, 2(1):189–226, 2000.

[43] V. Ziebart and P. Oliver. Mechanical properties of thin films from the load deflection of long clamped plates. *Journal of Microelectromechanical Systems*, 7(3):320–328, 1998.